Water Fat Separation with SSFP

Michael Mendoza

A thesis submitted to the faculty of
Brigham Young University
in partial fulfillment of the requirements for the degree of

Master of Science

Neal Bangerter, Chair
Brian Mazzeo
Scott Burt

Department of Electrical and Computer Engineering

Brigham Young University

December 2013

Copyright © 2013 Michael Mendoza

All Rights Reserved

ABSTRACT

Water Fat Separation with SSFP

Michael Mendoza
Department of Electrical and Computer Engineering, BYU
Master of Science

Magnetic resonance imaging (MRI) is an important medical imaging technique for visualizing soft tissue structures in the body. It has the advantage of being noninvasive and unlike x-ray does not rely on ionizing radiation for imaging. In traditional hydrogen-based MRI, the strongest measured signals are generated from the hydrogen nuclei contained in water and fat molecules. Reliable and uniform water fat separation can be used to improve medical diagnosis. In many applications the water component is the primary signal of interest, while the fat component represents a signal which can obscure the underlying pathology or other features of interest. In other applications the fat signal is the signal of interest. There currently exist many techniques for water fat separation. Dixon reconstruction techniques take multiple images acquired at select echo times with specific phase properties. Linear combinations of these images produce separate water and fat images.

Balanced steady-state free precession (bSSFP) MRI is a technique capable of producing images with high signal-to-noise ratio (SNR) in a short imaging time but suffers from signal voids or banding artifacts due to magnetic field inhomogeneity and susceptibly variations. These signal voids degrade image quality. Several methods have been developed to remove these banding effects. The simplest methods combine images across multiple bSSFP image acquisitions.

A technique in water fat separation was developed which combines the advantages of SSFP with Dixon reconstruction in order to produce robust water fat decomposition with high SNR in a short imaging time, while simultaneously reducing banding artifacts which traditionally degrade image quality. This algorithm utilizes four phased-cycled bSSFP acquisitions at specific echo times. Phase sensitive post-processing and a field map are used to prepare the data and reduce the effects of field inhomogeneities. Dixon reconstruction is then used to separate water and fat images.

Keywords: MRI, Magnetic Resonance Imaging, Fat Suppression, Water Fat Separation, Water/Fat Decomposition, Steady State Free Precession, SSFP, Dixon

ACKNOWLEDGMENTS

Thanks go to the ECEn style file authors for providing both a reasonable initial style and the motivation to abandon it. Yes!

Table of Contents

List of Figures ix

List of Tables xi

1 Introduction 1

- 1.1 Motivation . . . 1
- 1.2 Problem Overview . . . 2
- 1.3 Thesis Contributions . . . 3
- 1.4 Thesis Outline . . . 3

2 Principles of Magnetic Resonance Imaging 7

- 2.1 Introduction . . . 7
- 2.2 Physics of MRI . . . 7
  - 2.2.1 Nuclear Spin . . . 7
  - 2.2.2 Magnetization . . . 8
  - 2.2.3 Precession . . . 9
  - 2.2.4 Excitation . . . 11
  - 2.2.5 Relaxation . . . 12
  - 2.2.6 Bloch Equation . . . 14
- 2.3 Spatial Encoding . . . 15
  - 2.3.1 Slice-selective Excitation . . . 15
  - 2.3.2 Frequency and Phase Encoding . . . 16
- 2.4 MR Signal Detection and Image Reconstruction . . . 17

- 2.5 Non-Ideal Signal Variation . . . 18
  - 2.5.1 Magnetic Field Inhomogeneity . . . 18
  - 2.5.2 Chemical Shift . . . 18
  - 2.5.3 Image Noise . . . 19

3 Magnetic Resonance Imaging Simulation 21

- 3.1 Simulation Overview . . . 21
- 3.2 Virtual Tissue Model . . . 22
- 3.3 MRI Pulse Sequence . . . 22
- 3.4 Magnetization Simulation . . . 23
- 3.5 Modeling of Signal Variation . . . 25
- 3.6 MR Signal Generation and Image Reconstruction . . . 26

4 Steady State Free Precession 29

- 4.1 Introduction . . . 29
- 4.2 SSFP Spectra . . . 31
  - 4.2.1 SSFP Spectra Characteristics . . . 31
  - 4.2.2 Banding Artifacts . . . 32
  - 4.2.3 Phase-Cycling and Multiple-Acquisition Techniques . . . 32
- 4.3 SSFP Constrast . . . 33
- 4.4 SSFP Simulation . . . 33

5 Water-Fat Separation 37

- 5.1 Dixon Techniques . . . 37
  - 5.1.1 Two-Point Dixon . . . 38
  - 5.1.2 Phase Correction . . . 39
  - 5.1.3 Three-Point Dixon . . . 41
  - 5.1.4 Dixon Algorithm Limitations . . . 43

6 Water Fat Separation with SSFP 45
6.1 Algorithm Description 45
6.2 Parameter Selection 46
6.3 Simulation Results 49
    6.3.1 Comparison with Dixon Methods 49
    6.3.2 Noise and Field Inhomogeneity Analysis 49
    6.3.3 Algorithm Limitations 53
6.4 Discussion and Future Work 55

A Water-Fat Separation with SSFP Algorithm Psuedo-Code 57

References 59

List of Figures

2.1 Magnetic moments of hydrogen nuclei 9
2.2 Precession of magnetization vectors 10
2.3 Excitation of spins 11
2.4 Generation of phase error due of off-resonance effects 19

3.1 Block Diagram for MR Image Simulator 21
3.2 Water-Fat Phantom Tissue Model Mask 22
3.3 Basic Pulse Sequence Diagram 23

4.1 SSFP Pulse Sequence Example 30
4.2 SSFP Spectra 31
4.3 Phased-cycled SSFP spectra 33
4.4 SSFP Spectra for water and fat 34

5.1 Water fat separation using the two-point Dixon method 39
5.2 Water and fat separation using the two-point and three-point Dixon methods 41
5.3 Water and fat component estimates for water element 44
5.4 Phase error estimation and Water and fat component estimates error. . . . 44

6.1 SSFP phase-cycled off-resonance spectra adjusted for constant phase increase 47
6.2 Water fat separation using the SSFP Separation method 50
6.3 Wate 51
6.4 Water fat separation using SSFP separation method in the presence of noise and B_0 field inhomogeneity. 52

6.5 Water and fat separation using SSFP separation method in the presence of a large gradient field 54

List of Tables

2.1 Common T_1 and T_1 values 14

5.1 Effects of phase error on water image estimates 40

6.1 SSFP parameters used for water fat separation 46

6.2 Simulated SNR and CNR as a function of f_0 width in standard deviations . 53

6.3 Simulated SNR and CNR as a function of tip angle 53

Chapter 1

Introduction

Magnetic resonance imaging (MRI) is an important medical imaging technique for visualizing soft tissue structures in the body. It can show medical problems which can not be easily seen with other imaging methods such as x-ray, ultrasound, or computed tomography (CT) scans since it provides superior soft tissue contrast while maintaining good spatial resolution. MRI has the advantage of being noninvasive and unlike x-ray does not rely on ionization radiation for imaging and therefore presents no health risks under normal conditions. MRI functions by measuring the signal generated from the magnetic moments of certain nuclei while under the presence of a large magnetic field when excited by radio frequency pulses. Images of organs and biological structures in the body are generated from these signals and are used in medical diagnosis[7].

1.1 Motivation

In traditional hydrogen based MRI, the strongest measured signals are generated from the hydrogen nuclei contained in water and fat molecules. The separation of water and fat signals can be used to improve medical diagnosis. In some applications the water component is the primary signal of interest, while the fat component represents a signal which can obscure the underlying pathology or other features of interest. In other applications, the fat signal is the signal of interest; this includes studies of bone marrow, breasts, and the myocardial fatty tissue in the heart[6].

1.2 Problem Overview

Water fat separation in MRI is possible because of a property of MRI called the chemical shift. Under a large static magnetic field, the protons of water and fat molecules will resonate at slightly different frequencies. When these molecules are under a large static magnetic field and excited by a radio frequency pulse at a specific frequency, these molecules will generate signals at slightly different frequencies. The chemical shift is caused by the electronic environment of the nuclei which can cause a shielding of the magnetic field felt by these nuclei. This shielding is created by the orbital motion of nearby, surrounding electrons. Water molecules are relatively simple molecules which consist of two hydrogen atoms and one oxygen atom and experience little electronic shielding. Fat (or lipid) molecules, in contrast, consist of chains of carbons with many CH_2 groups which cause greater electronic shielding of the hydrogen molecules in the CH_2 groups. These electronic interactions cause the protons in fat to feel a weaker magnetic field, which causes its resonant frequency to be lower by about 3.5 parts per million with respect to water.

Water and fat separation as well as fat suppression techniques are an active area of research. There currently exist many techniques for water fat separation. Of particular interest to the research presented in this thesis are phase-sensitive techniques such as Dixon reconstruction. In Dixon reconstruction the signals generated by the hydrogen in water and fat molecules can be modeled by the following simplified signal equation:

$$s(t_n) = s_w + s_f e^{i\omega_f t_n} \tag{1.1}$$

where s_w is the signal amplitude for water, s_f is the signal amplitude for fat, t_n is the sample time also known as the echo time (TE) for the signal, s, and ω_f is the difference in resonance frequency between water and fat. Taking images at specific echo times allows the relative phase, $\theta = i\omega_f t_n$, between water and fat to be manipulated. Dixon reconstruction works by taking multiple images at specific echo times. Successive images are in-and-out of phase with respect to each other. Linear combinations of these images are then used to produce separate water and fat images.

1.3 Thesis Contributions

The main contributions of this thesis are the following:

- The development of a basic MRI simulation which involves every component of MR image formation, starting with basic MR physics, to generate a simulated MR image. This MRI simulation was used to understand SSFP and Dixon reconstruction, to analyze the effects of parameter variation on image formation, and to assist in algorithm development and optimization.
- The development of an algorithm for water fat separation which combines the advantages of SSFP (i.e., high SNR with a short scan time) with Dixon reconstruction. This algorithm does this while simultaneously reducing the regions of signal void known as banding artifacts which are a disadvantage of SSFP. The proposed method also attempts to reduce phase errors due to magnetic field inhomogeneities and susceptibility variations by use of a field map.

1.4 Thesis Outline

The remainder of the thesis is organized as followed:

Chapter 2: Principles of Magnetic Resonance Imaging

This chapter provides a basic theoretical background for magnetic resonance imaging. A review of basic MRI physics is given including the ideas of nuclear spin, magnetization, precession, excitation, and relaxation. The theory of spatial encoding and concepts of MR signal generation and detection are also introduced along with non-ideal sources of MR signal variation including the concepts of off-resonance, chemical shift, and image noise.

Chapter 3: Magnetic Resonance Imaging Simulation

The simulation of MRI is an important counterpart to the acquisition and processing of real MRI data. To assist in algorithm development and optimization, an MRI simulation was designed to simulate the generation of an MR image starting from the basic MR physics. This chapter provides an introduction to virtual tissue models, MRI pulse sequences, magnetization simulation, MR signal generation and image reconstruction as well as gives a simple description of this MRI simulation that was developed.

Chapter 4: Steady State Free Precession

Balanced Steady State Free Precession(bSSFP) is technique capable of producing images with high SNR in a short imaging time, but suffers from characteristic signal voids or banding artifacts due to B0 field inhomogeneity and susceptibility variations. This chapter describes theory and characteristics of bSSFP sequences. This includes the signal equations for SSFP, off-resonance spectra characteristics, the origin of banding artifacts, phase-cycling, and multiple acquisition techniques for reducing the effects of banding artifacts.

Chapter 5: Water Fat Separation

In traditional hydrogen based MRI, the strongest measured signals are generated from the hydrogen nuclei contained in water and fat molecules. Reliable and uniform water fat separation can be used to improve medical diagnosis. Dixon reconstruction is a set of phase-sensitive techniques for the decomposition of water and fat images. These techniques take advantage of chemical shift, which causes water and fat components to precess at slightly different frequencies. They do this by taking multiple images acquired at specific echo times with specific phase properties. Linear combinations of these images produce separate water and fat images. This chapter will outline this theory.

Chapter 6: SSFP with Water Fat Separation

The primary focus of the research presented in this thesis was to develop an algorithm which is capable of producing separate water and fat images by combining the advantages of SSFP (i.e. high SNR in a short scanning time) with Dixon reconstruction. This technique presented, which simultaneously separates water and fat while reducing SSFP banding, requires four phase-cycled bSSFP image acquisitions at select repetition times. This chapter gives a detailed explanation of the developed algorithm, as well as simulation results.

Chapter 2

Principles of Magnetic Resonance Imaging

2.1 Introduction

Nuclear magnetic resonance (NMR) is the foundation of magnetic resonance imaging (MRI). NMR is a physical phenomena in which atomic nuclei placed in a strong magnetic field absorb and re-emit electromagnetic radiation at a particular energy. The energy and frequency at which this electromagnetic radiation is generated depends on the strength of the applied magnetic field as well as the spin and magnetic properties of the nuclei in the field. In order to generate an image in MRI, an MR signal is obtained by placing the object of interest in a large magnetic field and exciting its nuclei with a radio frequency (RF) signal. This MR signal is spatially encoded with the use of linearly varying gradient fields. The received MR signal is processed to obtain the desired MR image. This chapter will outline the basic MR physics and imaging principles important for MR image formation[7].

2.2 Physics of MRI

2.2.1 Nuclear Spin

Spin is an intrinsic quantum mechanical property of electrons, protons, and neutrons. It is a form of angular momentum carried by these particles. Spin can only take on certain specific values. Intuitively, spin is often visualized as the angular momentum associated with a particle spinning about its axis, much like a spinning top. This simplistic model, while useful for visualization, is not entirely correct and should not be taken too literally. This notion, however, is adequate for many situations encountered in MRI physics. In reality, spin is a solely quantum-mechanical quantity that has no direct counterpart in classical mechanics. Despite this, it has a foundation in quantum theory and is measurable by experiment. The Stern-Gerlach experiment was the first experiment to infer its existence[1].

The magnetic dipole moment is a quantity induced by spin which is associated with atomic nuclei. This dipole moment, μ, makes the nucleus act like a tiny magnetic compass needle and is expressed by the product of the expected value of the spin angular momentum, S, with the gyromagnetic ratio, γ.

$$\mu = \gamma S \tag{2.1}$$

All isotopes that contain an odd number of protons and/or neutrons have a non-zero spin, while isotopes with an even number have a total spin of zero. Isotopes that have a non-zero spin will produce a non-zero magnetic moment and are capable of producing an NMR signal. Common isotopes of interest in MRI include ^{1}H and ^{23}Na. Hydrogen, in the form of water and various organic compounds, is one of the most abundant elements in organic tissue. Its most common isotope (^{1}H) is a spin 1/2 particle which exhibits a dipole moment and has a gyromagnetic ratio of $42.576/(2\pi)$ Mhz T^{-1} . This makes ^{1}H an important signal source in MR images of organic tissue[7].

2.2.2 Magnetization

Magnetization is a measure of the magnetic dipole moments in a material. In this formulation, we will define magnetization as the sum of magnetic moments in a volume of tissue.

$$M = \sum_{Vol} \mu \tag{2.2}$$

Normally, in the absence of a static magnetic field the directions of the magnetic moments in a material like ^{1}H are randomly distributed in a variety of directions and therefore their net

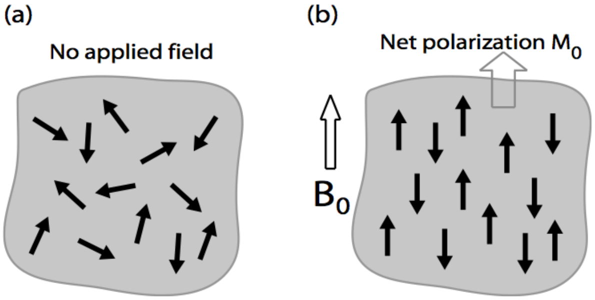

Figure 2.1: Magnetic moments of hydrogen nuclei. In the absence of a magnetic field, the directions of the magnetic moments are randomly distributed, as shown in (a). In the presence of a magnetic field, the magnetic moments will align, as shown in (b).

magnetization is zero. However, when placed in a large static magnet field their magnetic moments, like tiny compass needles, will feel the torque of the magnetic field. This will cause them to align and anti-align as shown in Figure 2.1. A net magnetization is created because slightly more magnetic moments will tend to align themselves.[7].

2.2.3 Precession

Precession is a change or wobble in the axis of orientation of a rotating body. It occurs when a torque is applied to a rotating object. While precession is often thought of occurring with spinning tops, it occurs with all rotating objects. This includes tops, wheels, astronomical bodies as well as magnetization of atomic nuclei in the presence of a magnetic field. The following will demonstrate the precession of magnetization in a B field[1, 7].

In order to show that precession occurs in the presence of a magnetic field, we will first start with spin angular momentum, S . Derived from quantum mechanics, the time evolution of the spin angular momentum is as follows

$$\frac{d\bar{S}}{dt} = \gamma\bar{S} \times \bar{B} \tag{2.3}$$

Multiplying both sides by the gyromagnetic ratio,γ, we can write the previous equation as a function of magnetic moment, μ

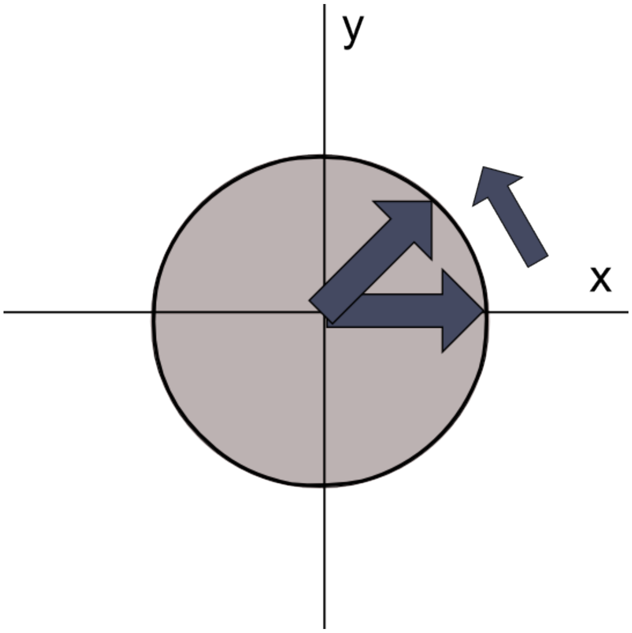

Figure 2.2: Precession of magnetization vectors in x-y plane with a strong B_0 field in z.

$$\frac{d\bar{\mu}}{dt} = \bar{\mu} \times \gamma\bar{B} \tag{2.4}$$

Then remembering that M is the summation of $\bar{\mu}$ over a volume we see that

$$\frac{d\bar{M}}{dt} = \bar{M} \times \gamma\bar{B} \tag{2.5}$$

This relationship is similar to the relation for the precession of a top in classical mechanics i.e.

$$\frac{de_z}{dt} = \omega \times e_z \tag{2.6}$$

where e_z is the direction of the central axis of the top and ω is the frequency of precession due to the torque supplied from gravity[11]. This similarity allows use to use a spinning top as an analogy for the precession of magnetization vectors.

For a spinning top, it is the angular momentum in the presence of gravity that causes precession about the direction of gravity. For magnetization, it is the magnetic moments in the presence of a magnetic field which cause precession about the direction of the field. The frequency of this precession is given by

$$\omega = \gamma B \tag{2.7}$$

This frequency of precession is known as the Larmor frequency. This frequency represents a resonant frequency of atomic nuclei and is the frequency at which a radio frequency (RF) pulse is applied in order to generate an MR signal.

2.2.4 Excitation

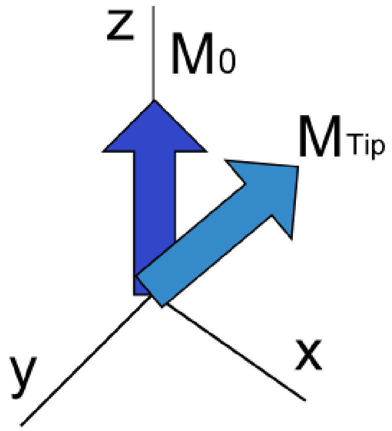

Figure 2.3: An RF pulse at Larmor frequency causes magnetic dipoles to "tip" out of their equilibrium position, M_0. This is equivalent to taking the magnetization vector M_0 and rotating it to M_{tip}

In NMR a radio frequency (RF) signal is used to "excite" the magnetic moments of the nuclei in the large static magnetic field, B_0. While the static field is used to align these magnetic moments, the RF pulse is used to rotate or "tip" these moments away from their equilibrium state. The equilibrium state of the magnetization vector is in the direction of the B_0 field. This RF pulse is tuned to the Larmor frequency and is aligned so that the magnetic field produced by the RF pulse, known as B_1, is applied in the transverse plane (x-y plane) in order to excite the magnetization vector out of equilibrium.

Essentially, B_1 applies a torque on the magnetization vector in order to rotate the vector. Mathematically this is equivalent to taking some magnetization vector, $\bar{M}$, and rotating this vector about the horizontal axis by α radians. This is done with the angle dependent rotation matrix $R_x(\alpha)$.

$$\bar{M}_{tip} = \bar{M} R_x(\alpha) \tag{2.8}$$

$$R_x(\alpha) = \begin{pmatrix} 1 & 0 & 0 \\ 0 & \cos(\alpha) & \sin(\alpha) \\ 0 & -\sin(\alpha) & \cos(\alpha) \end{pmatrix} \tag{2.9}$$

After excitation, the magnetization vectors will continue to precess at the Larmor frequency and will subsequently return back to their equilibrium positions. During this process called relaxation, the magnetic moments of the tissue will emit a measurable radio-frequency electromagnetic signal at the Larmor frequency. In NMR, this signal is detected with a radio-frequency receive coil. The detected signal is proportional to the magnetization in the transverse plane, M_{xy}, and is the source of the MR signal used to generate MR images.

2.2.5 Relaxation

Relaxation is a process in which the magnetization vectors return back to their equilibrium positions after excitation. Relaxation consists of two components: a longitudinal and transverse component. Longitudinal relaxation is the process of the longitudinal component, M_z, returning to its original equilibrium value. Transverse relaxation is the decay of the transverse component, M_{xy}. While the exact mechanism of relaxation is a complex process, the following simple phenomenological description will be sufficient for our purposes.

After relaxation the longitudinal component will recover exponentially back to its equilibrium value. This exponential behavior can be found to obey the following relationship

$$\frac{dM_z}{dt} = \frac{-M_z - M_0}{T_1} \tag{2.10}$$

whose solution is

$$M_z(t) = M_0 + (M_z(0) - M_0)e^{\frac{-t}{T_1}} \tag{2.11}$$

where M_z(t) is the longitudinal component of the magnetization vector at time t, $M_z(0)$ is the initial longitudinal component, M_0 is the magnitude of the magnetization vector at equilbrum and T_1 is a tissue dependent decay constant. T_1 is called the spin-lattice time constant and it used to describe the return of the magnetization to its equilibrium position along the direction of the B_0 field.

The magnitude of the transverse component of the magnetization vector corresponds to the magnitude of the MR signal. The behavior of this transverse component of the magnetization can be described by

$$\frac{dM_{xy}}{dt} = -\frac{dM_{xy}}{T_2} \tag{2.12}$$

whose solution is

$$M_{xy}(t) = M_{xy}(0)e^{\frac{-t}{T_2}} \tag{2.13}$$

where $M_{xy}(t)$ is the transverse component of the magnetization vector at time t, $M_{xy}(0)$ is the initial transverse component , and T_2 is tissue dependent decay constant. T_2 is called the spin-spin time constant and its used to describe the decay of the transverse component of the magnetization vector.

T_1 and T_2 are the time constants which characterize the relaxation of the magnetization vectors when they are not in their equilibrium state. Differences in these values are the

Tissue	$T_1(ms)$	$T_2(ms)$
grey matter	920	100
white matter	790	92
muscle	870	47
fat	270	85
kidney	630	58
liver	490	43

Table 2.1: Some T_1 and T_2 values for common organic tissues

primary source of image constraint in MR images. Common T_1 and T_2 values for common tissues can be found in Table 2.1.

2.2.6 Bloch Equation

The Bloch equation is a three dimensional phenomenological description of the dynamics of magnetization. It combines the concept of precession with the idea of transverse and longitudinal relaxation to describe how magnetization will evolve over time in the presence of magnetic fields. This equation is expressed as

$$\frac{d\bar{M}}{dt} = \bar{M} \times \gamma B + \frac{M_x\hat{\imath} + M_y\hat{\jmath}}{T_2} + \frac{(M_z - M_0)\hat{k}}{T_1} \tag{2.14}$$

where γ is the gyromagnetic ratio, T_1 is the spin-lattice (longitudinal) relaxation time constant, T_2 is the spin-spin (transverse) relaxation time constant, M_0 is the equilibrium magnetization due to the main B_0 field, and $\hat{\imath}$, $\hat{\jmath}$, $\hat{k}$ are the unit vectors in the x,y, z directions respectively.

This equation can be solved to give an approximate time evolution for magnetization in the presence of magnetic fields. In MR image generation, there exist three magnetic fields of interest. These are:

1. The static main field, B_0
2. The field from the radio frequency pulse used for excitation, B_1
3. The gradient fields used for spatial localization, G(t)

It important to note that each of these magnetic fields plays an crucial part in MR image formation. The static B_0 field causes the magnetization vectors to align in the direction of the field and dictates the frequency needed for the RF pulse to excite the nuclear spins. The B_1 field is generated from the RF pulse and is used to produce the energy for the nuclei to absorb and then re-emit as electromagnetic radiation at the same frequency. This electromagnetic radiation is read by an RF receive coil and constitutes the MRI signal used to generate an MR image. The gradient fields, $G(t)$, are used for spatial localization will be described in the following section.

2.3 Spatial Encoding

In order to generate images in MRI, a body is placed into an MRI scanner. This scanner generates a large static magnetic field across the tissues to be imaged with a large superconducting solenoidal magnet. As mentioned earlier, in the presence of this field, the magnetization vectors will align. Then when the scan begins, an RF transmit coil will emit an RF pulse in order excite the spins. This will cause the spins to precess and a signal will be emitted for a set of receive coils to measure. This received signal will be the sum of all the signals emitted from the spins in the body. Now in order to generate an image, spatial localization is required in order to isolate each voxel in the body being imaged. This is accomplished with a set of coils in the scanner which generate linear magnetic gradient fields into order to spatially encode each voxel. The spatial encoding is completed through a combination of three methods: slice-selective excitation, frequency encoding and phase encoding.

2.3.1 Slice-selective Excitation

Slice-selective excitation is a method used to isolate a slice of tissue in the xy-plane. This isolation is accomplished by modifying the main B_0 field in the z-direction with the z-gradient coil to cause linear variations in the Larmor frequency in the z-direction. This means that the spins will resonate at different frequencies depending on the local magnetic field felt where the local field is: $B(z) = B_0 + G_z z$. Using an RF pulse tuned to the Larmor frequency of the main B_0 field, different signals are received depending on the strength of the G_z field. When the z-gradient coil is off, the whole volume of spins is excited and the received signal will be the sum of all the signals emitted from the spins in the body. However when the z-gradient coil is active, only spins located near the location in the z-direction where the local magnetic field is equal to B_0 field will be excited and emit a signal. All other locations will not be excited and will not generate an MR signal. This creates a signal which is the sum of all the signals emitted from the spins located in the slab only. This effectively isolates a slab of tissue in the z-direction.

2.3.2 Frequency and Phase Encoding

Frequency and phase encoding is used to isolate a pixel from a slice of tissue which has already been isolated by slice-selective excitation. This is accomplished by modifying the local magnetic fields with a set of spatially varying gradient fields in both the x and y directions at different times. After being encoded, the MR signal of each pixel in the slice can be later recovered to generate an image of the slice.

Frequency encoding is used to encode the MR signal in the x - direction. This is done by applying a gradient in the x - direction while the MR signal is being sampled. This causes the local spins in the x direction to precess with varying frequency and consequently emit MR signals at different frequencies. This encodes the local measured signal in the x -direction with different frequencies.

Phase encoding is used to encode the MR signal in the y - direction. This encoding is created by applying a gradient field in the y - direction (G_y) for a specific amount of time prior to the sampling an MR signal. During the application of the G_y the local spins in the y - direction will precess at different frequencies, and after the gradient is removed, they will have accumulated different amounts of phase. The difference in phase in y - direction is called phase encoding.

2.4 MR Signal Detection and Image Reconstruction

In MR imaging, a series of slice-selective excitations, phase encodings, and frequency encodings concurrent with signal sampling are used to generate all the information necessary to reconstruct an image. The MR signal is sampled using an RF receiver coil. This received signal is the sum of the signals emitted from the nuclear spins in the body and comes from the transverse component of the magnetization. As such the received signal can be expressed as

$$s(t) = \int \int m(x,y) e^{-i\gamma \, (\int_0^t G_x(\tau) d\tau) \, x \, (\int_0^t G_y(\tau) d\tau) \, y} \, dx \, dy \tag{2.15}$$

where m(x,y) is the transverse magnetization and the exponential terms represents the phase accrued due to the gradient fields in the x and y directions from frequency and phase encoding. Rewriting the signal equation in terms of a Fourier transform gives

$$\begin{aligned} s(t) &= \int \int m(x,y) e^{i2\pi[k_x(t)x + k_y(t)y]} \, dx \, dy \\ k_x(t) &= \tfrac{\gamma}{2\pi} \int_0^t G_x(\tau) d\tau \\ k_y(t) &= \tfrac{\gamma}{2\pi} \int_0^t G_y(\tau) d\tau \end{aligned} \tag{2.16}$$

where k represents spatial frequency-variation in frequency space, also called “k-space”. Now in order to reconstruct an image from measured MR signal, we take the inverse Fourier transform of $m(x,y)$. This reconstruction method is possible because the MR signal equation is equivalent to the 2D transform of $m(x,y)$ [7].

2.5 Non-Ideal Signal Variation

In an ideal world an MR image would be free of any imperfections which could degrade image quality, unfortunately this is not the case. There are, in reality, a number of factors which can cause the measured MR signal to deviate from the theory presented thus far. These include the effects from deviations in the static B_0 field known as magnetic field inhomogeneity, changes in precession frequency due to the chemical shift, and signal noise.[2]

2.5.1 Magnetic Field Inhomogeneity

Unfortunately, due to manufacturing limitations, it is impossible to design and fabricate a magnet which is perfectly uniform. While we try to generate a perfectly uniform B_0 field, there will always be small variations in the magnetic field. These variations in the B_0 field are known as magnetic field inhomogeneity. These variation, while small, will cause some nuclear spins to resonance at frequencies different from the Larmor frequency of the B_0 field and introduce phase error into the MR imaging process [7].

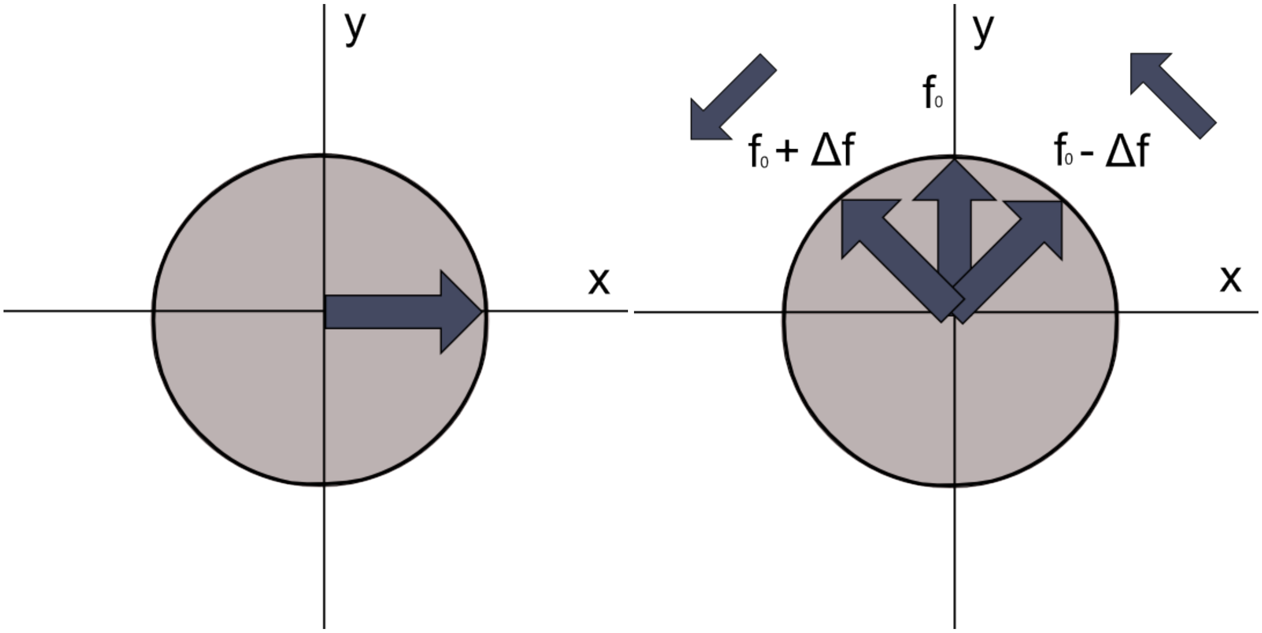

Figure 2.4: Generation of phase error due of off-resonance effects like B_0 inhomogeneity and the chemical shift. (Left) Magnetization vector at t=0, (Right) Mangetization vector at some t=Δt later. Note that magnetization vectors at different frequencies will have accumulated different amounts of phase during Δt time. This is due to off resonance effects.

2.5.2 Chemical Shift

Another source of image phase error is caused the chemical shift. The chemical shift occurs because protons of water and fat molecules will produce signals with slightly different resonant frequencies when excited by the same magnetic field. It is caused by differences in a proton's electronic environment due to the shielding created by the orbital motion of surrounding electrons. This shielding causes a decrease in the effective magnetic field felt by each nuclei. Since resonant frequency is proportional to the magnetic field felt, this causes a corresponding decrease in the resonant frequency.

Water molecules are a simple molecule which consist of two hydrogen and one oxygen and experience little electronic shielding. Fat (lipid) molecules, in contrast, consist of chains of carbons with many CH2 groups which cause electronic shielding of the hydrogen molecules within the CH2 groups. These electronic interactions cause the protons in fat to feel a weaker magnetic field, which causes its resonant frequency to be lower by about 3.5 parts per million with respect to water. For a 3T magnet, this corresponds to a shift in resonant frequency of about 428 Hz [7].

2.5.3 Image Noise

In the acquisition of MR images noise is always present, which is why it is important to acquire images with a strong signal in order to be able to resolve biological structures and features in the body. The main sources of noise in MRI comes from random electrical fluctuations in the imaging subject and electrical noise from the receive coil. Since the measured MR signals contain both magnitude and phase information, image noise is modeled as complex zero-mean Gaussian process [2].

Chapter 3

Magnetic Resonance Imaging Simulation

The simulation of MRI is an important counterpart to the acquisition and processing of real MRI data. Simulation can be used as an educational tool for gaining a theoretical understanding of MR technology, as well as a helpful tool in the development and optimization of new MRI algorithms. In the development of algorithms, simulation allows the user to isolate the causes and effects of image artifacts in MRI and offers an environment from which the user can quickly run simulated MR experiments and analyze the effects of parameter changes have on image formation. To assist in algorithm development and optimization, an MRI simulation was designed to simulate the generation of an MR image starting from the basic MR physics outlined previously.

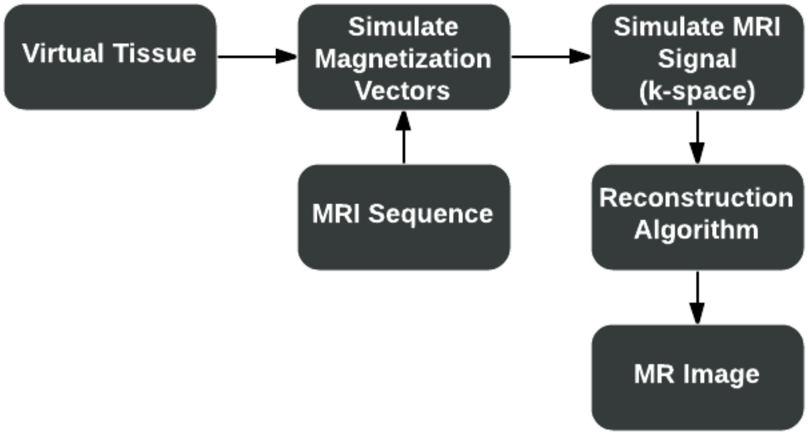
Virtual Tissue
Simulate Magnetization Vectors
Simulate MRI Signal (k-space)
MRI Sequence
Reconstruction Algorithm
MR Image

Figure 3.1: Block Diagram for MR Image Simulator

3.1 Simulation Overview

This basic MRI simulation involves every component of MR image formation, starting with the basic MR physics of the Bloch equation, to generate a simulated MR image. A block diagram of the system's architecture is show in Figure 3.1. The procedure for generating an image begins with a virtual tissue model and a MRI pulse sequence which are then used to compute the time evolution of the tissue model's magnetization vectors. A simulated MR signal is generated from these magnetization vectors, and then the received signal is reconstructed using a fast Fourier transform (FFT) to form a simulated image.

3.2 Virtual Tissue Model

A virtual tissue model is a discrete, simulated description of a real nuclear spin system for a biological tissue. Each tissue model consists of a set of tissue elements which represent each voxel located in the tissue model. Each of these tissue elements contains the set of physical parameters necessary to compute the local spin magnetization from the solutions to the Bloch equations. These parameters include the the proton density, ρ, the longitudinal relaxation constant, T_1, the transverse relaxation constant, T_2 and the off-resonance frequency of the tissue element, f_0. In addition to these parameters, a local B_0 field inhomogeneity parameter, ΔB, is attached to each tissue element.

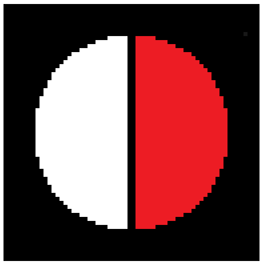

Figure 3.2: Water-Fat Phantom Tissue Model. This tissue model was used to model a 2D slice of a water-fat phantom. This simulated tissue slice has the water region located on the left, and the fat region on the left and contains 64 x 64 tissue elements.

3.3 MRI Pulse Sequence

During an MRI scan, an object is placed into a large magnetic field and is then excited by a number of coordinated actions. This set of coordinated actions is called an MRI pulse sequence. A typical MRI pulse sequence, as shown in Figure 3.3, consists of the timings of an ordered combination of RF and gradient pulses. Typically, a pulse sequence consists of a series of excitation RF pulses separated by a set repetition time, TR. Gradient pulses are then used to select a 2D slice from a 3D volume and to spatially encode the MRI data. This data is recorded at a specific time called the echo time, TE, during sampling window which is designated by the readout pulse in the diagram. This simulator uses a pulse sequence to schedule a set of RF pulses and gradient pulses for use in the simulation.

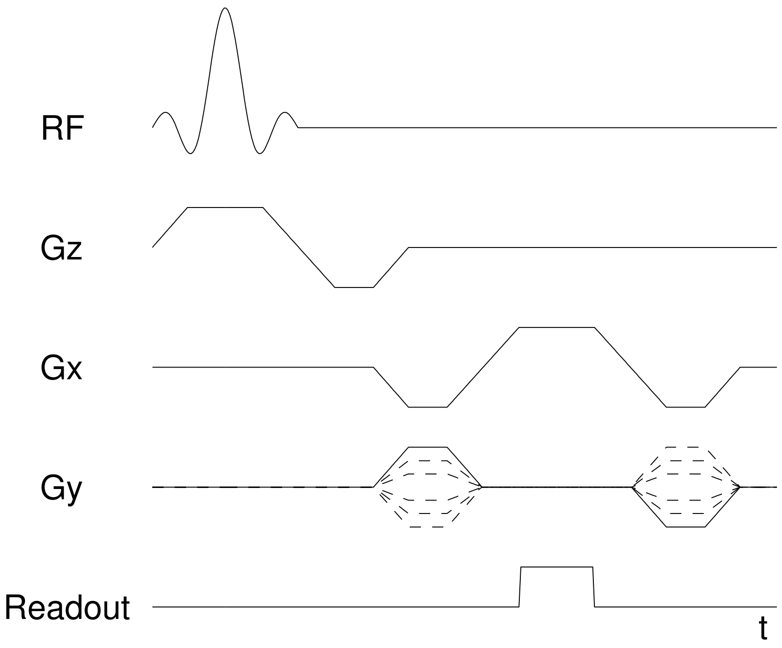

Figure 3.3: MRI Pulse Sequence Diagram.

3.4 Magnetization Simulation

The simulation of the magnetization of each tissue element in a tissue model is done by computing solutions to the Bloch equation. These solutions are computed discretely in time according to the supplied pulse sequence. The magnetization of each subsequent time step, $M(x, t + \Delta t)$, is dependent on the previous step's magnetization at the same location as well as the magnetic fields of the pulse sequence. These fields affect the magnetization through a series of rotation and exponential scaling factors according to

$$M(x, t + \Delta t) = f(R_{RF}, R_{relax}, R_{precess}, R_{off} M(x, t)) \tag{3.1}$$

where R_{RF} represents the effect of the excitation of the nuclear spins by an RF pulse, R_{relax} represents the effects of relaxation, $R_{precess}$ represents the effects of precession, and R_{off} represents the effects of off-resonance.

The first factor, R_{RF}, represents a rotation of the magnetization vectors due to the excitation of the nuclear spins by an RF pulse. This simulation supports a number of RF pulses. The simplest supported model for an RF pulse is an α degree tip of a magnetization vector about the x-axis. This is expressed as the following rotation matrix

$$R_{RF}(\alpha) = \begin{pmatrix} 1 & 0 & 0 \\ 0 & \cos(\alpha) & \sin(\alpha) \\ 0 & -\sin(\alpha) & \cos(\alpha) \end{pmatrix} \tag{3.2}$$

The second component to the time evolution of the magnetization vectors, R_{relax}, models the effects of longitudinal and transverse relaxation. This component is derived by solving the Bloch equations and is given by

$$\mathbf{M}(t+\Delta t) = \begin{pmatrix} e^{-\Delta t/T_2} & 0 & 0 \\ 0 & e^{-\Delta t/T_2} & 0 \\ 0 & 0 & e^{-\Delta t/T_1} \end{pmatrix} \mathbf{M}(t) + \begin{pmatrix} 0 \\ 0 \\ M_0(1-e^{-\Delta t/T_1}) \end{pmatrix} \tag{3.3}$$

The third component models the effects of off resonance precession, caused by a variety of imposed magnetic field sources, on the magnetization. These sources include the gradient fields (G_x, G_y, G_z), and magnetic field inhomogeneities, ΔB. The combined magnetic field of these sources is given by

$$B(x,y,z) = G_x x + G_y y + G_y z + \Delta B \tag{3.4}$$

Since magnetic fields affect the resonance frequency (i.e. $\omega = \gamma B$) this allows the effects of precession on the magnetization vector to be modeled as

$$R_{precess} = e^{-i\omega\Delta t} \tag{3.5}$$

where

$$\omega(x,y,z) = \gamma(\int_0^t G_x x d\tau + \int_0^t G_y y d\tau + \int_0^t G_z z d\tau + \Delta B) \tag{3.6}$$

The final component models the effects off-resonance precession, due to the chemical shift, on the magnetization. This can be modeled by a extra amount of rotation in the x-y plane. The extra about of precession in the x-y planes in a time Δ t is given by

$$R_{off}(\beta) = \begin{pmatrix} \cos(\omega_{off}\Delta t) & \sin(\omega_{off}\Delta t) & 0 \\ -\sin(\omega_{off}\Delta t) & \cos(\omega_{off}\Delta t) & 0 \\ 0 & 0 & 1 \end{pmatrix} \tag{3.7}$$

where ω_{off} is the difference in resonance frequency due to the chemical shift.

In the MRI simulation, these factors are combined together in order to generate the magnetization for the next time stop. Starting from a set of initial parameters the magnetization vectors for each of the tissue elements are interactively computed.

3.5 Modeling of Signal Variation

Since there exist a number of sources of non-ideal signal variation in MR signal generation, the MRI simulation contains a module to simulate these effects. This module is capable of modeling magnetic field inhomogeneity effects, off-resonance effects due to the chemical shift, and signal noise.

- Magnetic field inhomogeneities are handled as an extra magnetic field term in the precession component of the magnetization simulation.
- Off-resonance effects are handled by giving each species a Gaussian off-resonance profile in ω_{off}. A standard deviation parameter determines the width of this profile.
- Noise is modeled as complex zero-mean Gaussian random variance. This complex noise has a real and an imaginary component. Each component is model to be independent and to have the same variance. For the simulation, noise is added after the computation of the magnetization vectors when the signal is sampled.

3.6 MR Signal Generation and Image Reconstruction

Thus far, we have used the the solutions to the Bloch equations to simulate the magnetization vectors of a simulated tissue. Now we will show how to generate an MR signal from these simulated magnetization vectors. In MR imaging, an RF receiver coil is designed and used to measure electromagnetic radiation which is emitted after an RF pulse is applied to the body. This received signal is the sum of the signals emitted from the nuclear spins in the body and comes from the transverse component of the magnetization. Therefore, the received signal, $s(t)$, can be written as

$$s(t) = \int_x \int_y \int_z M_{xy}(x, y, z, t) dx\, dy\, dz \tag{3.8}$$

where the transverse magnetization is defined as

$$M_{xy}(x, y, z, t) = M_x(x, y, z, t) + iM_y(x, y, z, t) \tag{3.9}$$

In order to understand how to reconstruct an image from the received MR signal we will simplify this signal equation. First, to acquire a 2D image, we will integrate over the width of 2D slice. This gives the signal for a 2D slice of magnetization in the transverse plane. Next, we will absorb all the components of the magnetization except for the factors related to the gradient fields into $m(x, y)$. Taking these steps, we can now rewrite the signal equation as

$$s(t) = \int \int m(x, y) e^{-i\gamma\, (\int_0^t G_x(\tau) d\tau)\, x\, (\int_0^t G_y(\tau) d\tau)\, y}\, dx\, dy \tag{3.10}$$

This equation says that the received signal is a function of the transverse magnetization and the phase accrued due to the gradient fields in the x and y directions from to frequency and phase encoding.

From here we can see that in order to recover an image from the received signal, we need to recover m(x,y) from s(t). Comparing the signal equation with the 2D Fourier transform of m(x,y)

$$\mathcal{F}(k_x, k_y) = \int \int m(x, y) e^{i2\pi[k_x(t)x + k_y(t)y]}\, dx\, dy \tag{3.11}$$

and doing a one-to-one correspondence with k_x and k_y, we can see that received signal can be expressed as

$$s(t) = \int \int m(x, y) e^{i2\pi[k_x(t)x + k_y(t)y]}\, dx\, dy \tag{3.12}$$

where

$$\begin{aligned} k_x(t) &= \tfrac{\gamma}{2\pi} \int_0^t G_x(\tau) d\tau \\ k_y(t) &= \tfrac{\gamma}{2\pi} \int_0^t G_y(\tau) d\tau \end{aligned} \tag{3.13}$$

From this we can see that the received signal is equivalent to the value of the 2D Fourier transform of m(x,y). Which means that an inverse Fourier transform can be used in order to recover m(x,y) from the received signal. In the MRI simulator, an algorithm known as an inverse fast Fourier (iFFT) transform is used to compute the inverse Fourier transform and reconstruct the desired image.

Chapter 4

Steady State Free Precession

Fully-refocused, or balanced, steady state free precession (SSFP) is a class of MRI techniques which are capable of achieving high signal-to-noise (SNR) in a short scan time when compared to other methods. This chapter will present an overview of the fundamental concepts of SSFP, and demonstrate the current techniques for generating images.

4.1 Introduction

A typical pulse sequence diagram for SSFP is shown in Figure 4.1. This pulse sequence demonstrates the timings of radio frequency (RF) pulses with respect to the gradient fields in the x, y, and z directions. In SSFP, RF pulses are continuously applied with a set repetition time (TR) between each pulse. After a large number of pulses are applied (i.e. > 100) the MR signal is sampled on an interval centered at an echo time (TE) with respect the last RF pulse.

Examining the signal magnitude closely between excitations, it can be observed that during the sampling window, the signal will exhibit transient behavior or fluctuations. After a period of time (several times longer than the longest T_1 present in the tissue), the signal magnitude will reach a steady state level. This is when the MR signal will be sampled.

As explained earlier, the applied gradient fields are important for spatial localization and are *fully-refocused* to eliminate any phase accumulation and therefore the effects on spin precession from excitation to excitation. This is accomplished by designing the gradient fields to integrate to zero between excitations as shown in Figure 4.1.

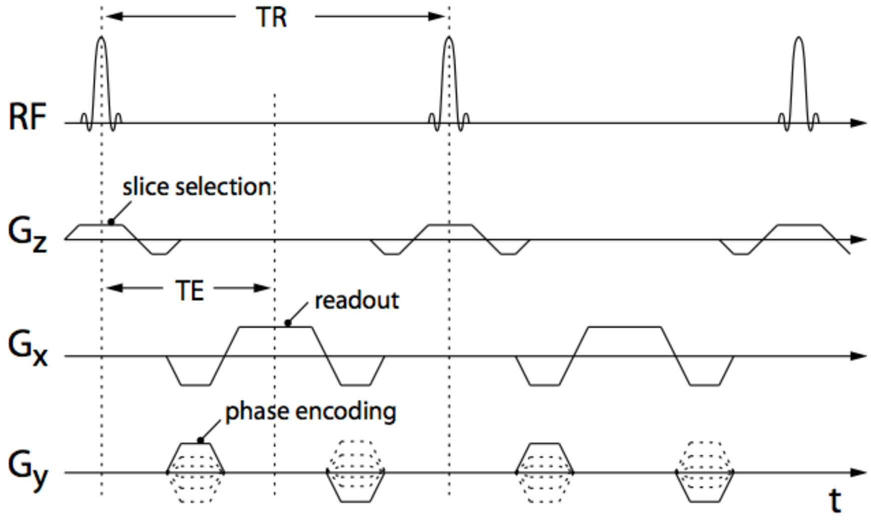

Figure 4.1: Pulse Sequence for SSFP

Typically TR values are chosen between 2 ms and 12 ms depending on application. In order to achieve a relatively constant phase profile, the sampling window is centered at $TE = TR/2$. For the most common tissues, T_2 values are in the range of 40 - 100 ms and T_1 value are typically in the hundreds of milliseconds. Comparing the TE values of SSFP to these T_2 and T_1 values, it can be seen that is only a small amount of time for spin relaxation is allowed between excitations. This relatively short TE allows the generation a of high SNR signal (often 30% higher than other steady-state MRI techniques). The short TR allows for fast scan times[2].

4.2 SSFP Spectra

The MR signal of SSFP sequences exhibits a strong dependance on precession frequency. If a tissue's precession frequency is off from the Larmor frequency, then the difference in precession frequency is called its off-resonance frequency. By varying the off-resonance frequency of the pulse sequence, one can generate a SSFP off-resonance spectrum. An example of a SSFP

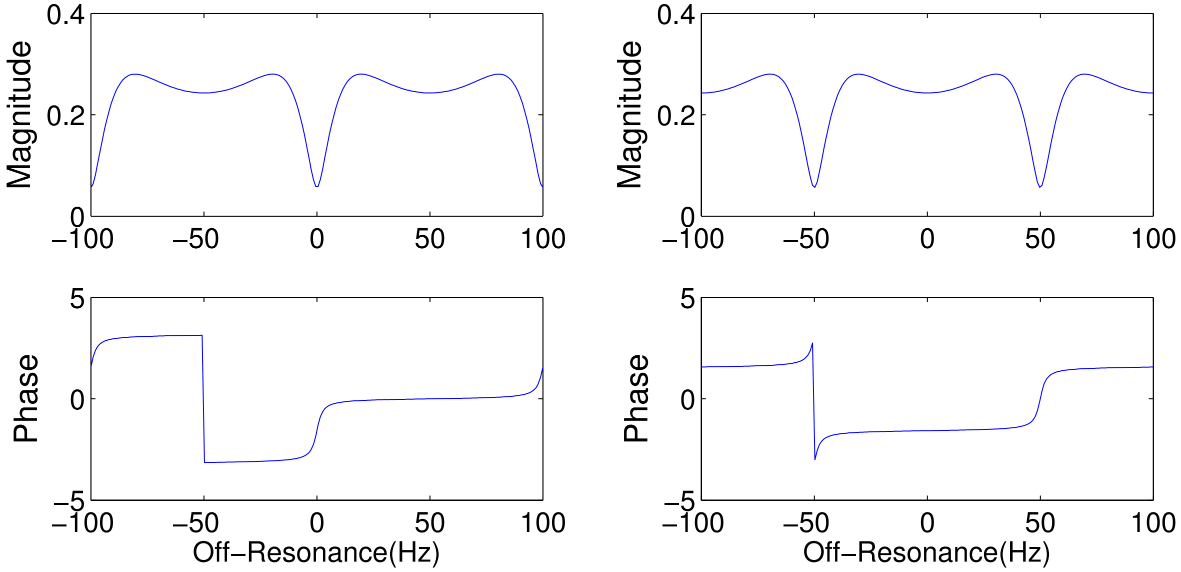

Figure 4.2: SSFP Spectra

spectrum is shown in Figure 4.2. Note that the spectrum is periodic in frequency and consists of a passband region and a null region of low signal level.

4.2.1 SSFP Spectra Characteristics

Figure 4.2 shows a series of typical single-acquisition SSFP off-resonance spectra for several tissues. These spectra are periodic in off-resonance frequency and are a strong function of off-resonance frequency. These spectra typically contain a pass band region with a strong periodic null in frequency. These signal nulls are the source of the off resonance banding artifact which we hope to remove. The signal phases shown in Figure 2 assume TE = TR/2. Note for this echo time (TE), the phase is relatively flat across the pass band region and rapidly changes at the signal nulls. Use of TEs other than TE = TR/2 generates a linear phase profile as opposed to the flat pass band characteristic of a SSFP sequence with TE = TR/2. Subsequent pass bands are 180° out of phase. In addition, for each tissue the shape of its SSFP signal is dependent on the tissue properties, T1 and T2. The SSFP spectra shown in Figure 4.2 each utilize an SSFP sequence with increasing RF phase from excitation to excitation which causes the off-resonance profile to be shifted by a corresponding amount in frequency in comparison to a SSFP sequence with a constant RF phase. This shift in the off-resonance spectra makes it possible to take multiple SSFP acquisitions in order to create a more homogeneous off-resonance spectrum without signal nulls as shown in Figure 4.3. These spectra were created by combining multiple SSFP images using the complex sum of the signals.

4.2.2 Banding Artifacts

While SSFP is capable of generating high SNR images in a short amount of time, it is also not without its limitations. One of the main disadvantages of SSFP is its high sensitivity to field inhomogeneity which is the is source of banding artifacts found in SSFP images. Banding artifacts are regions in the image where signal nulls are observed. These artifacts are most likely to occur in regions of high field variation, where the strong dependance on precession frequency may cause the region to cross multiple signal nulls in the SSFP spectrum.

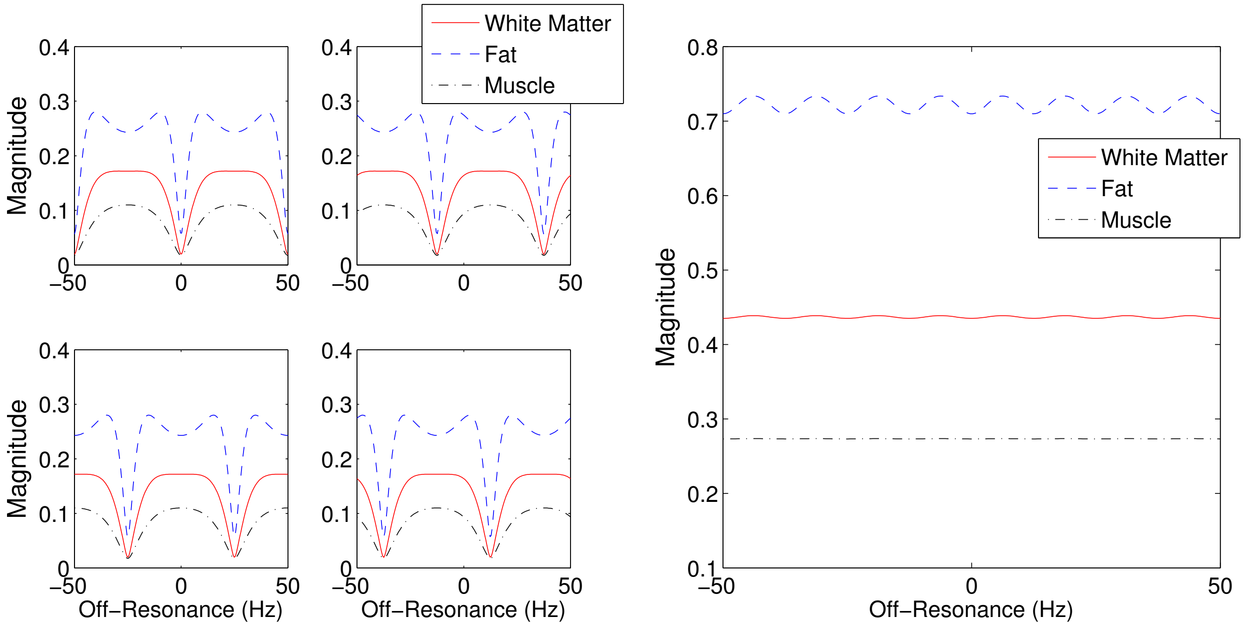

Figure 4.3: Four SSFP phase-cycled off-resonance spectra. (Left) Four phase-cycled spectra for $\delta\phi = 0$, $\pi/2$, π, $3\pi/2$ for various tissues. Note the shifting of the spectral profiles by $\delta\phi$ for each case. (Right) Four phased-cycled spectra are combined using the complex sum of the signals to create a more homogenous signal.

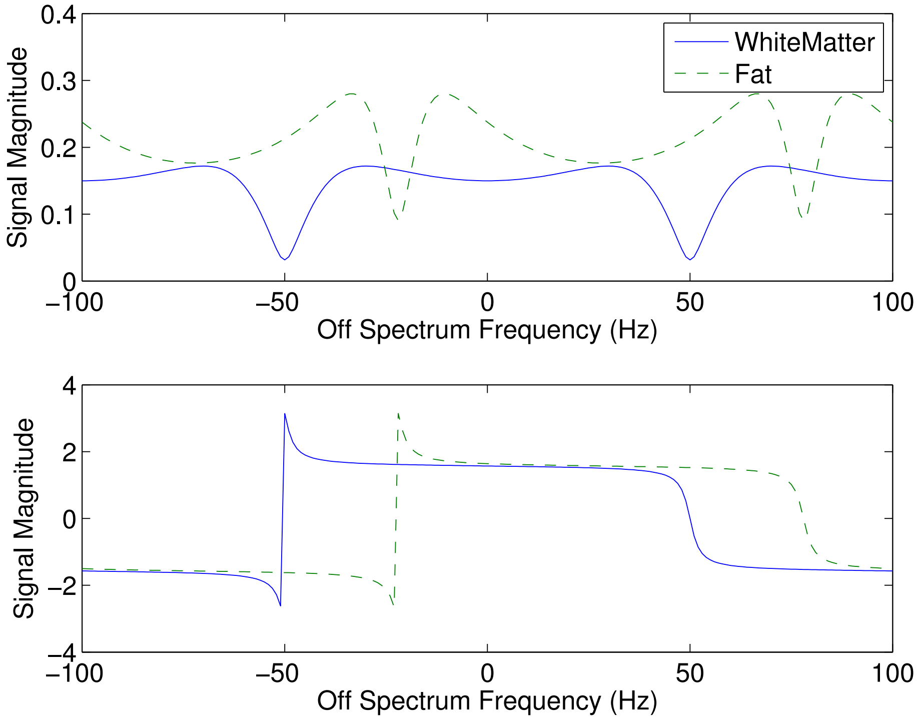

Figure 4.4: SSFP Spectra for water-based tissue and fat. These spectra were generated using the a SSFP simulation where the proton concentration was the same for both tissues. Note that SSFP generates a strong fat signal relative to water.

4.2.3 Phase-Cycling and Multiple-Acquisition Techniques

Phase-cycling is a useful technique in SSFP which allows a SSFP spectrum to be shifted in frequency. This shift in the spectrum is created by incrementing the phase of the RF pulse, ϕ, by a constant value of $\delta\phi$ from excitation to excitation. This will cause a corresponding $\delta\phi$ shift in spectrum as well as the addition of a constant phase to spectrum phase.

One application of phase-cycling is the removal of banding artifacts found in SSFP from images. These artifacts can be removed by taking multiple phase-cycled images each with a shifted spectral profile and combining these images in order to reconstruct the original image; thereby removing the banding artifact and improving the image's SNR.

4.3 SSFP Constrast

Contrast in SSFP for different tissues is a complicated function of T_2/T_1. Where this function becomes a topic of interest in the comparison of water-based tissues verse fat. As can be seen by Figure 4.4, SSFP generates a strong fat signal relative to water when all parameters other than T_1 and T_1 are the same.

4.4 SSFP Simulation

The simulation of an SSFP sequence is based on the solutions the 3D Bloch equation outlined in the previous chapter. We will begin with an initial magnetization vector where $\overline{M} = (M_x, M_y, M_z)^T = (0, 0, M_0)^T$ for some initial M_0 which is the initial magnetization of the tissue in the main B_0 field. We will then apply an RF pulse which will tip the magnetization vector by α degrees and advance its phase by ϕ. This is equivalent to

$$\mathbf{M}_{tip} = \mathbf{M} R_x(\alpha, \phi) \tag{4.1}$$

where $R_x(\alpha, \phi)$ is a rotation matrix given by

$$R_x = \begin{pmatrix} \cos(\alpha)\sin^2(\phi) + \cos^2(\phi) & (1 - \cos(\alpha))\cos(\phi)\sin(\phi) & -\sin(\alpha)\sin(\phi) \\ (1 - \cos(\alpha))\cos(\phi)\sin(\phi) & \cos(\alpha)\cos^2(\phi) + \sin^2(\phi) & \sin(\alpha)\cos(\phi) \\ \sin(\alpha)\sin(\phi) & -\sin(\alpha)\cos(\phi) & \cos(\alpha) \end{pmatrix} \tag{4.2}$$

After the tip the magnetization is affected by T_1 recovery and T_2 relaxation and off-resonance precession

$$\mathbf{M} = P(\beta) \begin{pmatrix} M_{tip}(x) e^{-TR/T_2} \\ M_{tip}(y) e^{-TR/T_2} \\ M_0 + (M_{tip}(z) - M_0) e^{-TR/T_1} \end{pmatrix} \tag{4.3}$$

where the T_1 recovery and T_2 relaxation are described by the first term and the additional precession about the z-axis is described by the rotation matrix $P(\beta)$. The amount of off-resonance phase accumulated across a TR is given by β. This represents the amount of additional precession in a TR.

$$P(\beta) = \begin{pmatrix} \cos(\beta) & \sin(\beta) & 0 \\ -\sin(\beta) & \cos(\beta) & 0 \\ 0 & 0 & 1 \end{pmatrix} \tag{4.4}$$

After excitation, relaxation and off-resonance precession, the phase of the RF pulse is incremented by $d\phi$ and the rotation matrix is recalculated, i.e. $R_x(\alpha, \phi) = R_x(\alpha, \phi + \delta\phi)$. This will allow for phase-cycling in the SSFP simulation, which will be explained in a subsequent section. This entire process constitutes one cycle of the SSFP sequence. This cycle is repeated multiple times until steady state is reached. Then the magnetization vector is excited one last time and allowed to relax and precess until TE where the signal is sampled. M_{TE} constitutes the magnetization vector at the time of sampling.

$$\mathbf{M}_{TE} = \begin{pmatrix} M_{tip}(x)e^{-TE/T_2} \\ M_{tip}(y)e^{-TE/T_2} \\ M_0 + (M_{tip}(z) - M_0)e^{-TE/T_1} \end{pmatrix} P(\beta \cdot TE/TR) \tag{4.5}$$

Algorithm 1 SSFP Algorithm

```
procedure SSFP($M_0$, $\alpha$, $\phi$, $\delta\phi$, $\beta$, TR, TE, $T_1$, $T_2$, $N_r$)
    $\mathbf{M} = (0, 0, M_0)$                                  ▷ Set Initial Magnetization
    for $N_r$ do                                                ▷ For each excitation
        $\mathbf{M_{tip}} = \mathbf{M}Rx(\alpha, \phi)$                        ▷ Tip Magnetization Vector
        $\mathbf{M}(t = TR) = P(\beta)\,\mathbf{M_{relax}}(TR)$              ▷ Process and Relax Magnetization
        $R_x(\alpha, \phi) = R_x(\alpha, \phi + \delta\phi)$               ▷ Increment $\delta\phi$ for Phase-Cycling
    end for
    $\mathbf{M_{tip}} = \mathbf{M}Rx(\alpha, \phi)$                            ▷ Tip Magnetization Vector
    $\mathbf{M}(t = TE) = P(\beta \cdot TE/TR)\,\mathbf{M_{relax}}(TE)$      ▷ Precess and Relax Magnetization
    return $M_{xy} = M(x) + iM(y)$                             ▷ Return Transverse Magnetization
end procedure
```

Chapter 5

Water-Fat Separation

In MR imaging, there are many applications which require reliable and uniform fat suppression for accurate medical diagnoses. In traditional MR images, fat is a bright signal which can obscure underlying pathology or other features of interest in tissues. It is therefore desirous to remove the fat signal from the image. Applications which require the removal of fat from images are often called fat suppression or water fat separation algorithms.

There currently exist a number of techniques for water fat separation in MRI. These techniques include Dixon techniques, iterative techniques such as IDEAL as well as many others [4, 5, 9, 10].

5.1 Dixon Techniques

Dixon reconstruction is a set of simple separation techniques which take advantage of the chemical shift, or the difference in resonance frequency, between water and fat signal components. Due to the chemical shift, it is known that water and fat precess at slightly different frequencies. This means there will be times at which their magnetization vectors will be aligned, or in-phase, and other times in which they will be anti-aligned, or out-of-phase. Dixon reconstruction takes advantage of this notion by acquiring multiple images at select echo times in order to generate "in-phase" and "out-phase" images and then uses linear combinations of these images in order to produce separate water and fat images[9].

5.1.1 Two-Point Dixon

The two-point Dixon method for water-fat separation is a simple method which uses only two images [4]. For this analysis it is assumed that only water and fat are present. If m_w is the water image, and m_f is the fat image, then the combined image for a specific amount of phase accruement due to off resonance precession, θ is

$$m_i = m_w + m_f e^{i\theta_i} \tag{5.1}$$

where we assume for simplicity and without loss of generality that we are on the resonance of water in the rotating frame so that only fat will precess the addition ω_f. The phase accruement (θ) is a function of off-resonance frequency of fat with respect to water (ω_f) and the echo time ($T_{E,i}$).

$$\theta_i = \omega_f T_{E,i} \tag{5.2}$$

In order to separate the images we select echo times such that the water component is out of phase with the fat component or in other words such that $\theta = \theta_2 - \theta_1 = \pi$. Equation 5.3 shows the equations for two images where $\theta_1 = 0$ and $\theta_2 = \theta = \pi$; this gives two images where the water and fat components are in phase in the first image and then out of phase in the second image.

$$\begin{aligned} m_1 &= m_w + m_f \\ m_2 &= m_w + m_f e^{i\theta} = m_w - m_f \end{aligned} \tag{5.3}$$

Now with these two images, assuming no phase error, it is a simple matter to separate water from fat. To recover the water or fat images all that is required is to either add or subtract the images. The resultant image is shown in Figure 5.1.

$$\begin{aligned} \hat{m_w} &= \tfrac{1}{2}[m_1 + m_2] \\ \hat{m_f} &= \tfrac{1}{2}[m_1 - m_2] \end{aligned} \tag{5.4}$$

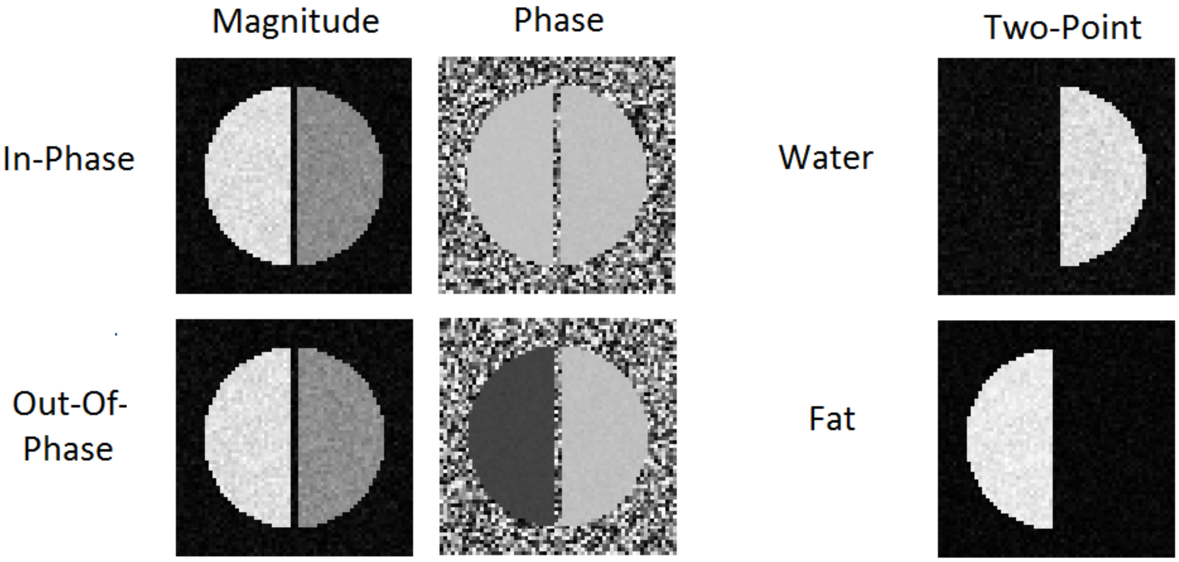

Figure 5.1: Water fat separation using the two-point Dixon method. (Left) The magnitude and phase for two simulated MR images which contain water and fat. One image is the “in-phase” image and the other is the “out-of-phase” image. (Right) Resultant water and fat separated images using two-point Dixon.

5.1.2 Phase Correction

The two-point Dixon method for water fat separation is a simple but effective method under ideal conditions. However, in the presence of noise or phase errors due to B_0 inhomogeneity this method can fail. The following is an analysis of the effects of phase error on water-fat decomposition.

In order to quantify the effects of phase errors (represented by ϕ) on the two-point Dixon method, we will add a phase error term then separate the images into their respective water and fat components. The following relationship adds a phase error term to the images used in the two-point Dixon reconstruction

$$\begin{aligned} m_1 &= (m_w + m_f) \\ m_2 &= (m_w - m_f)\, e^{i\phi} \end{aligned} \tag{5.5}$$

Using these relationships for m_1 and m_2 we solve for our estimates of m_w and m_f. This now gives us a relationship which describes the effects of phase error on water fat separation.

ϕ	$\hat{m_w}$	$\hat{m_f}$
0	1	0
$\pi/8$	0.9808	0.1951
$\pi/4$	0.9239	0.3827
$\pi/2$	0.7071	0.7071
π	0	1

Table 5.1: Effects of phase error on water image estimates, $\hat{m_w}$, from two-point Dixon method

$$\begin{aligned} \hat{m_w} &= \tfrac{1}{2}[m_1 + m_2] = \tfrac{1}{2}(m_w(1 + e^{i\phi}) + m_f(1 - e^{i\phi})) \\ \hat{m_f} &= \tfrac{1}{2}[m_1 - m_2] = \tfrac{1}{2}(m_w(1 - e^{i\phi}) + m_f(1 + e^{i\phi})) \end{aligned} \tag{5.6}$$

Inserting various values for ϕ shows that it only takes a small amount of phase error for the separation to lose its fidelity. A summary of these results are shown in Table 5.1. By adding a $\pi/8$ phase error between images, the water image estimate is left relatively unchanged; however the fat image is contaminated by almost 20%. By adding a phase error of $\pi/4$ that error in the fat image increases to almost 40%. And if a phase error of π is introduced, the water and fat images will swap.

5.1.3 Three-Point Dixon

The three-point Dixon method, developed by Glover in 1991, was developed as an extension to the two-point Dixon method which adds a simple first order correction for B_0 inhomogeneity [5]. This correction helps to eliminate phase errors in the reconstruction, but is not without its limitations. Techniques like IDEAL which utilize iterative least squares regressions in order to correct for B_0 inhomogeneity offer improved performance, at a cost of increased complexity. For this project the three-point Dixon was utilized due to its simplicity and sufficient separation performance for our application.

This technique uses two images which are “in-phase” and “out-of-phase” in order to separate water from fat. However, unlike the two-point method, this technique requires a third image in order to generate a simple B_0 inhomogeneity field map. A comparison of the

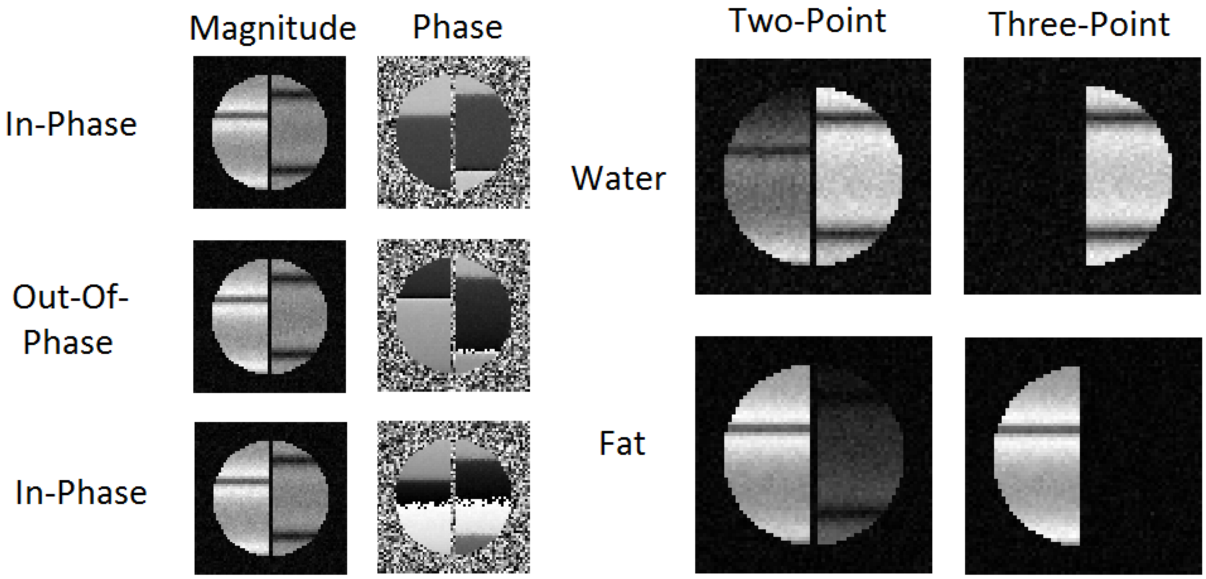

Figure 5.2: Water fat separation using the two-point and three-point Dixon methods. Selected images are SSFP simulated images taken with an added linear gradient added in the y direction. (Left) The magnitude and phase for three simulated MR images which contain water and fat. Two images are the “in-phase” images and one is the “out-of-phase” image. (Right) Resultant water and fat separated images using two-point Dixon and three-point Dixon. Note that the two-point method was unable to separate the images without error due to phase variation across the image, while the three-point method was able to successfully separate the images.

results from the two-point and the three-point Dixon methods is shown in Figure 5.2 and Figure 5.3. In this example for the three-point Dixion method, selected SSFP images were taken with an added linear gradient in the y direction in order to introduce a phase variation across the image. This illustrates that, the three-point method is capable of separating water from fat despite the phase variance across the image, while the two-point Dixon was unable to.

The following will outline the mathematics of the three-point Dixon algorithm. In the three-point Dixon method three images are required at select echo times. These selected echo times are used to create a set of MR images which represent an in-phase image, an out-of-phase image and a final in-phase image. For this derivation m_1, m_2, and m_3 will represent the three images to be used. In addition to these images, m_w, m_f, and 2ϕ will respectively represent the water component, the fat component and the phase difference between the two in-phase images, m_1 and m_3. For this example it is assumed, that B_0 inhomogeneity is constant between the images and that the time between each image is the same so that phase accumulated between the images, ϕ, is equal.

$$\begin{aligned} m_1 &= (m_w + m_f) \\ m_2 &= (m_w - m_f)e^{i\phi} \\ m_3 &= (m_w + m_f)e^{i2\phi} \end{aligned} \tag{5.7}$$

In order to generate a simple B_0 field map estimate, ϕ, the average total phase difference between the first and third image is calculated. This done as follows

$$2\hat{\phi} = \angle m_1^* m_3 \tag{5.8}$$

After generating a B_0 field map, the estimate of the separate water and fat components is simply

$$\begin{aligned} \hat{m_w} &= \tfrac{1}{2}[m_1 + m_2 e^{-i\hat{\phi}}] \\ \hat{m_f} &= \tfrac{1}{2}[m_1 - m_2 e^{-i\hat{\phi}}] \end{aligned} \tag{5.9}$$

5.1.4 Dixon Algorithm Limitations

Dixon reconstruction is rather robust technique in the presence of small magnetic inhomogeneities. However, in the presence of large magnetic inhomogeneities the phase errors become too great and the technique fails. Figures 5.3 and 5.4 shows the effects of phase error due to field inhomogeneity on water and fat component estimates for both the 2-point and 3-point Dixon reconstruction methods. For the 2-point Dixon method, the component estimates are a continuous function of phase error with good estimates for small phase errors. For the 3-point Dixon method, the component estimates are the correct component as long as the phase error is less than $\pi/2$. As soon as the phase error exceeds $\pi/2$ phase wrapping occurs in the field map estimate and the water and fat images swap.

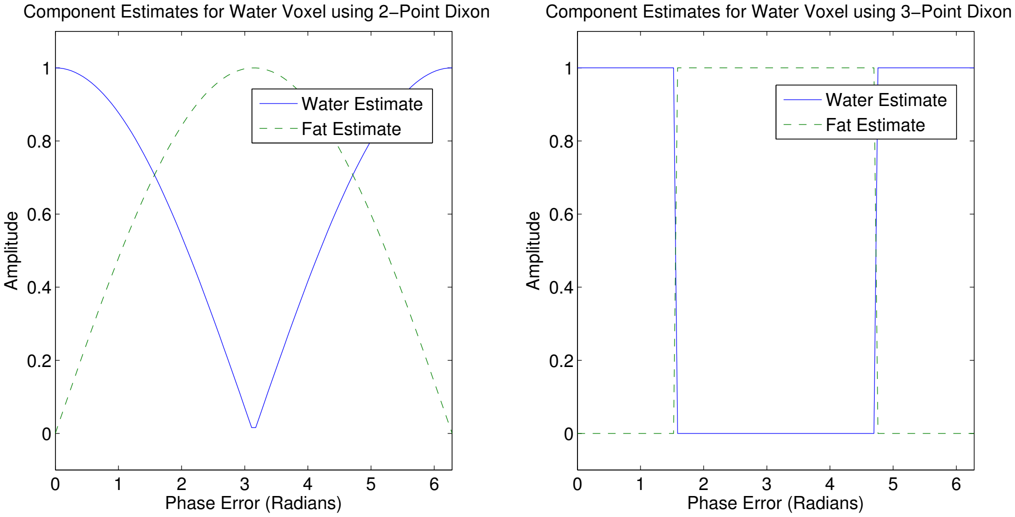

Figure 5.3: Water and fat component estimates for a water element. (Left) Component estimates for 2-point Dixon. (Right) Component estimates for 3-Point Dixon.

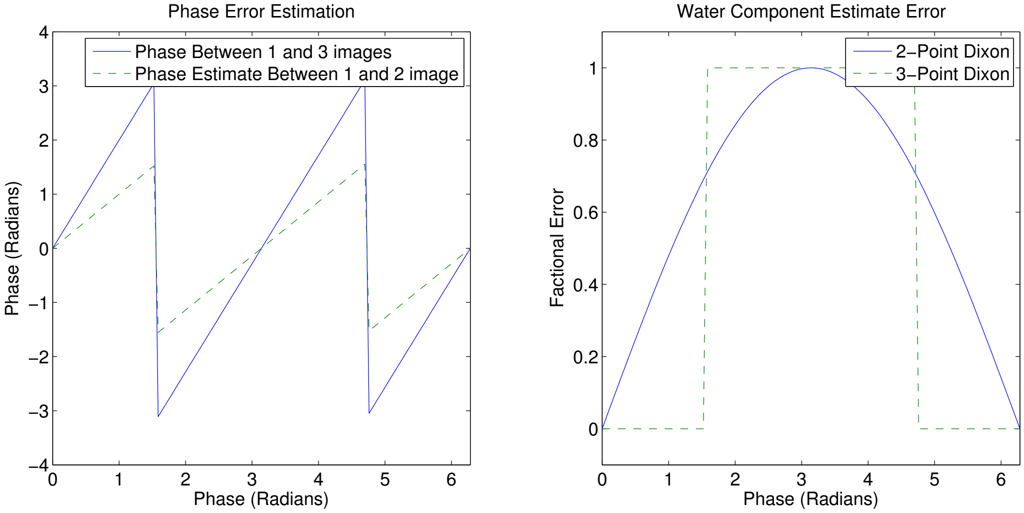

Figure 5.4: (Left) Phase due to magnetic inhomogeneity estimates. (Right) Water and fat component estimate error.

Chapter 6

Water Fat Separation with SSFP

The focus of this thesis was the development of a new technique for water fat separation in MRI. This technique combines steady state free precession (SSFP) and Dixon techniques for water fat suppression in order to generate images with high SNR in a short scan time. The basic idea of this technique is to take four phase-cycled SSFP images at select echo times and then process and combine these images in order to reconstruct separate water and fat images. These resultant images are free of the banding artifacts which are common in SSFP and are robust in the presence of noise and B_0 inhomogeneities.

The following will outline the algorithm for the new technique, and show the results from simulated data using this method for water fat separation.

6.1 Algorithm Description

The SSFP separation method is a novel technique for water fat separation. This technique combines SSFP with Dixon reconstruction in order to generate separate water and fat images. (Detailed psuedo-code which outlines the procedure for water fat separation is given in Appendix A.) The algorithm itself is relatively simple and consists of the following five steps:

1. Generate four phase-cycled images at select $\delta\phi$, ϕ and TE
2. Select three signals with the highest signal magnitudes from these four images
3. Modify the magnitude of the selected signals. The new magnitude for each signal is an average of the selected top three signals.

Image	$\delta\phi$	ϕ	TE	Simulation TE Value (ms)
1	0	0	$\frac{TR}{2} - \frac{3\Delta t_f}{2}$	3.2477
2	$\pi/2$	$-\pi/4$	$\frac{TR}{2} - \frac{\Delta t_f}{2}$	4.4159
3	π	$-\pi/2$	$\frac{TR}{2} + \frac{\Delta t_f}{2}$	5.5841
4	$3\pi/2$	$-3\pi/4$	$\frac{TR}{2} + \frac{3\Delta t_f}{2}$	6.7523

Table 6.1: SSFP parameters used for water fat separation

4. From the modified signals, select both an "In-Phase" and "Out-Of-Phase" image with the highest magnitude for its respective category (i.e. "In-Phase" and "Out-of-Phase")
5. Use 2-point Dixon reconstruction on these two images to generate separate water and fat images

Following this outlined procedure will generate separate water and fat images. Each of these five steps is done on a pixel by pixel basis, except for the original phase-cycled SSFP image generation.

6.2 Parameter Selection

The parameters selected for generation of the four phased-cycled images used for the algorithm are shown in Table 6.1. Each of these parameters is selected for a specific reason based on the effect each parameters has on the SSFP spectrum.

The parameter for the amount of phase increment between successive RF pulses, $\delta\phi$, controls the location of the signal nulls across a period of the SSFP spectrum. The four values of $\delta\phi$ are selected in order to evenly spread out the locations of the signal nulls relative to each SSFP image as shown in Figure 6.1. This is done so that none of the selected top three signals will contain a signal null. This is important because across a signal null there exists large phase change which makes an image region with a bad candidate for phase sensitive techniques. Therefore, it is important that the selected signals, which will ultimately use Dixon methods for water fat separation, do not contain a signal null. Also when combining these selected images, using a complex or magnitude sum, the resultant image will have even more reduced banding effects than combining all images.

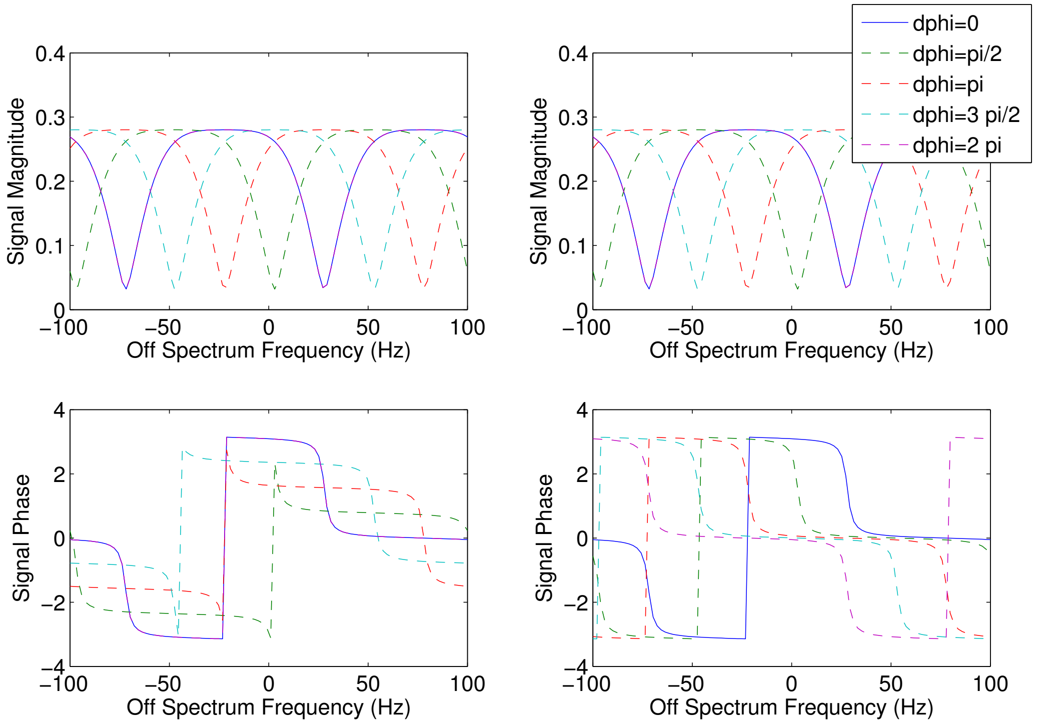

Figure 6.1: SSFP phase-cycled off-resonance spectra adjusted for constant phase increase. (a:Left) Five phase-cycled spectra for $\delta\phi = 0, \pi/2, \pi, 3\pi/2, 2\pi$ for a simulated fat tissue. Note the shifting of the spectral profiles between each phase-cycle by $\delta\phi$ and the additional constant phase between each phase-cycle. (b:Right) Five phase-cycled spectra for $\delta\phi = 0, \pi/2, \pi, 3\pi/2, 2\pi$ and $\phi = 0, -\pi/4, -\pi/2, -3\pi/4, -\pi$. Note a negative ϕ is used for each phase-cycle. These specific ϕ are used to remove the constant phase gained between phase-cycles due to increasing $\delta\phi$ between each phase-cycle.

The parameter for the starting RF pulse phase, ϕ, controls how much constant phase to add across an SSFP image. The values for ϕ were selected to remove the constant phase gained between phase-cycles due to increasing $\delta\phi$ between each phase-cycle. Without these specific values of ϕ the phase of the SSFP images would not be properly aligned across the images. Figure 6.1a shows the effect of having phase-cycled images without using ϕ to correct for the constant phase difference between the images. Note that the phase between the phase-cycled spectrums is not aligned. Figure 6.1b shows the effect of having phase-cycled images with using ϕ to for correct the constant phase differences across the images. Note that the phase between the spectrums is aligned in areas without signal null (i.e. the phases only have a 0 or π difference between them).

The last parameter of interest to this discussion is the echo time (TE). The echo time effects the relative phase between the water and fat components in a SSFP image. For example, take an image with an echo time ($TE = TE_0$) where the water and the fat images are "In-Phase", meaning their phases are equal. Take a second image at a latter TE time ($TE = TE_0 + \Delta t$). In this image the water and fat will have a different relative phase since fat precesses slower than water due to the chemical shift. How different the relative phase is depends on the time between successive images (Δt) and the difference in the resonance frequencies between water and fat. Using a 3T magnet, this difference in resonant frequency is 428Hz. This means that the time, Δt, it takes for the relative phases to get "Out-of-Phase" is 1.1682 milliseconds. Therefore, in order to generate images which are successively "In-Phase", "Out-of-Phase", "In-Phase" and "Out-of-Phase" there must be a time difference of $\Delta t = 1.1682$ ms between each successive image.

In addition, to effects on relative phase, the echo time can effect the shape of a SSFP phase profile. Choosing an echo time that is half the repetition time (TR) ensures that there is a relatively constant phase profile in the SSFP spectrum. Selecting another echo time adds an extra linear phase to the SSFP spectrum. Since it is necessary to have echo times which are not $TR/2$, the echo times in Table 6.1 are selected in order to minimize the effects of having TE not equal to $TR/2$.

6.3 Simulation Results

The following section will present the simulated results for water fat separation with SSFP algorithm presented in this chapter.

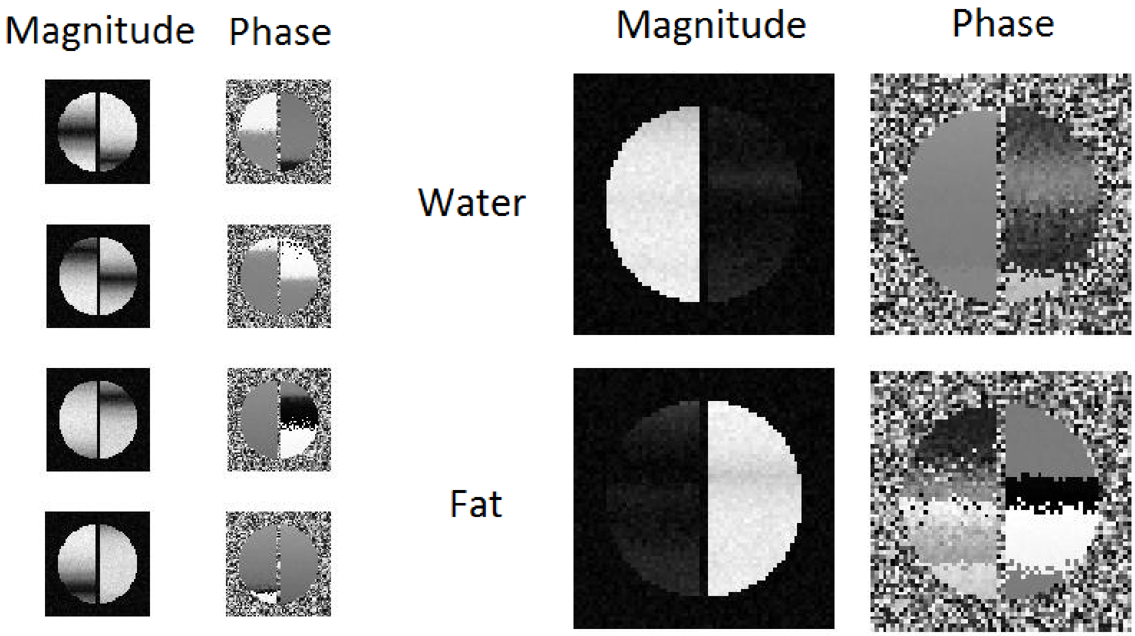

Figure 6.2: Water fat separation using the SSFP separation method. Selected images are SSFP simulated images taken with an added linear gradient in the y direction. (Left) The magnitude and phase for four phase cycled simulated MR images which contain water and fat (for $\delta\phi = 0$, $\pi/2$, π, $3\pi/2$). Two images are "in-phase" images and two are "out-of-phase" images. (Right) Resultant water and fat separated images using the SSFP separation method.

Figure 6.2 shows the results of using water fat separation using the SSFP separation method. As can be seen, the algorithm is capable of separating water and fat images with relatively high fidelity, despite the presence of banding artifact in each of the original SSFP images. It is worthwhile to note, that magnitude images show little evidence of signal ripple while the phase images have bands of different signal phase. These bands of phase are evidence that multiple combinations of images where used to compose this resultant image.

6.3.1 Comparison with Dixon Methods

Figure 6.3 shows the results of the two-point, three-point and SSFP separation methods on water fat separation. In this example, the selected images were taken with an added linear gradient in the y direction in order to introduce multiple banding artifacts as well as a large phase variation across the image. As can be seen, the SSFP separation method greatly out preforms the two-point and the three-point Dixon methods. The Dixon methods, which only utilize information from two or three of the phase-cycled SSFP images, tend to fail in regions on or near regions of signal null where the phase variation is too great. The SSFP separation method is able to success where the Dixon methods.

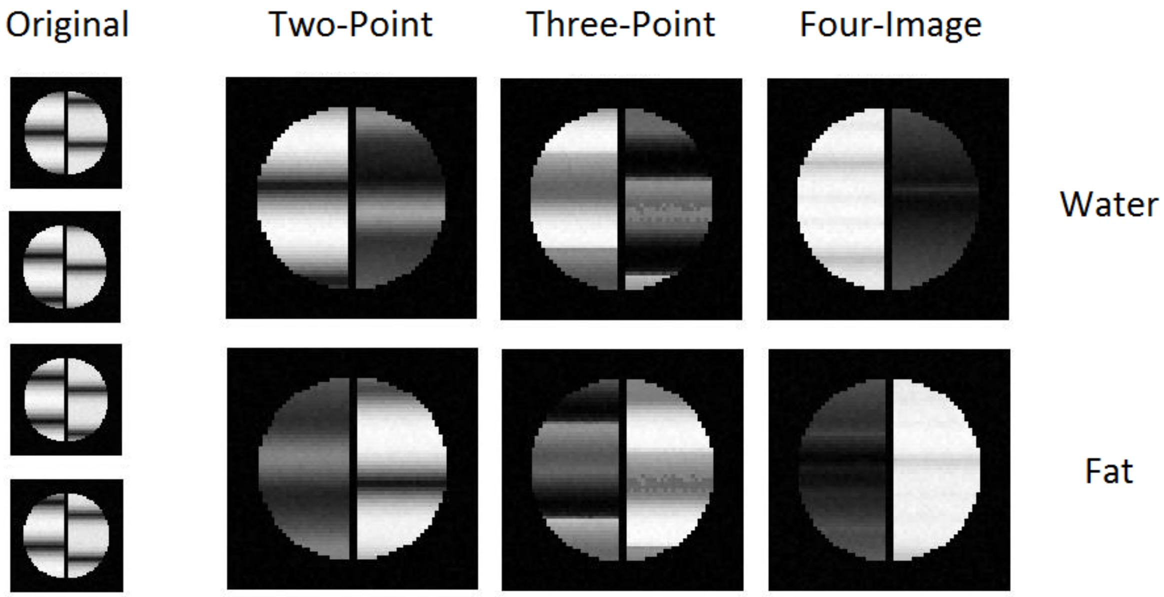

Figure 6.3: Water fat separation using the two-point Dixon, three-point Dixon, and SSFP separation methods.

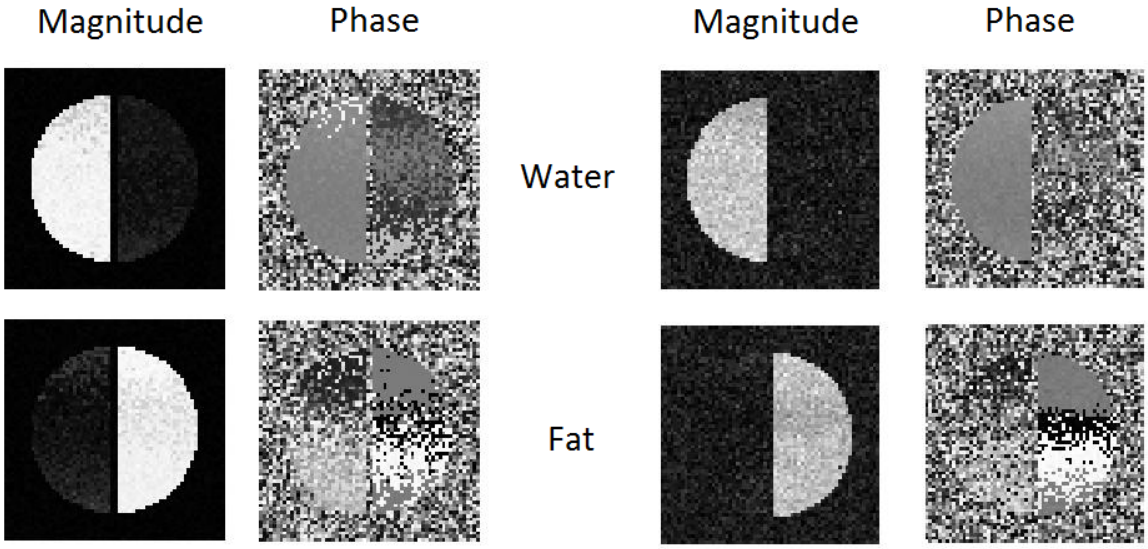

Figure 6.4: Water fat separation using SSFP separation method in the presence of noise and B_0 field inhomogeneity. (Left) Water and fat separated images in the presence of moderate noise. (Standard deviation of the noise equal to about 15 percent of fat and water signal.) (Right) Water and fat separated images in the presence of randomly distributed B_0 inhomogeneity (Standard deviation of frequency change (Δf) due to inhomogeneity is 10 Hz).

6.3.2 Noise and Field Inhomogeneity Analysis

A simulated noise and field inhomogeneity analysis was done using the SSFP separation method in order to better understand the limitations of this algorithm. Table 6.2 and Figure 6.4 show results of adding a random about field inhomogeneity to the tissue model. As can be seen, in the presence of small-moderate field inhomogeneity the algorithm appears to performs well. Also with increasing field inhomogeneity the algorithm appears to maintain a good separation and a consistent, strong image contrast between water and fat images. Figure 6.4 also shows the results of adding a moderate noise source. In the presence of noise, the algorithm appears to maintain a good separation between water and fat components.

f_0 σ	Water SNR	Fat SNR	Water CNR	Fat CNR
0.0	130.7619	125.9524	118.7619	113.7619
1.0	130.7143	126.0000	118.7143	113.5714
2.0	130.7143	125.9524	118.7143	113.5714
10.0	130.3333	126.1429	118.0000	112.8095
20.0	129.4762	126.5714	115.1429	111.1429
30.0	128.4762	126.8571	111.9048	108.3333

Table 6.2: Simulated SNR and CNR as a function of f_0 width in standard deviations.

α	Water SNR	Fat SNR	Water CNR	Fat CNR
$\pi/3$	130.7619	125.9524	118.7619	113.7619
$\pi/4$	151.4762	127.5714	142.2381	115.8095
$\pi/5$	159.1429	112.9048	138.3810	102.2381
$\pi/6$	159.0476	76.6190	101.0000	66.1905
$\pi/7$	155.0476	57.6190	79.0000	46.2857
$\pi/8$	145.2857	46.6667	59.5714	26.8571

Table 6.3: Simulated SNR and CNR as a function of tip angle (α).

6.3.3 Algorithm Limitations

The SSFP separation method appears to separate water and fat images well in the presence of noise and moderate magnetic field inhomogeneity. However, the algorithm is not with out its disadvantages.

The first limitation of the SSFP separation algorithm is a function of tip angle. In order to function well, the SSFP separation algorithm requires a SSFP spectrum with a single peak. At smaller tip angles the SSFP spectrum begins to develop multiple signal peaks and the signal wobbles in the passband region. This shape change in the SSFP spectrum beings to occur at tip angles less than or equal to $\pi/5$. So it is not surprising that the algorithm begins to fail at tip angles less than or equal to $\pi/5$. Table 6.3 shows the SNR and CNR as function of tip angle. Note that at tip angles less than $\pi/5$ the contrast between water and fat images drops rapidly.

The second limitation of the SSFP separation algorithm is related to how strong of a gradient field is placed across a tissue sample. In the presence of a small to moderate field gradient the algorithm appears to function well. However, in the presence of a strong extra field gradient the algorithm begins to fail. This evidence of this effect is shown in Figure 6.5.

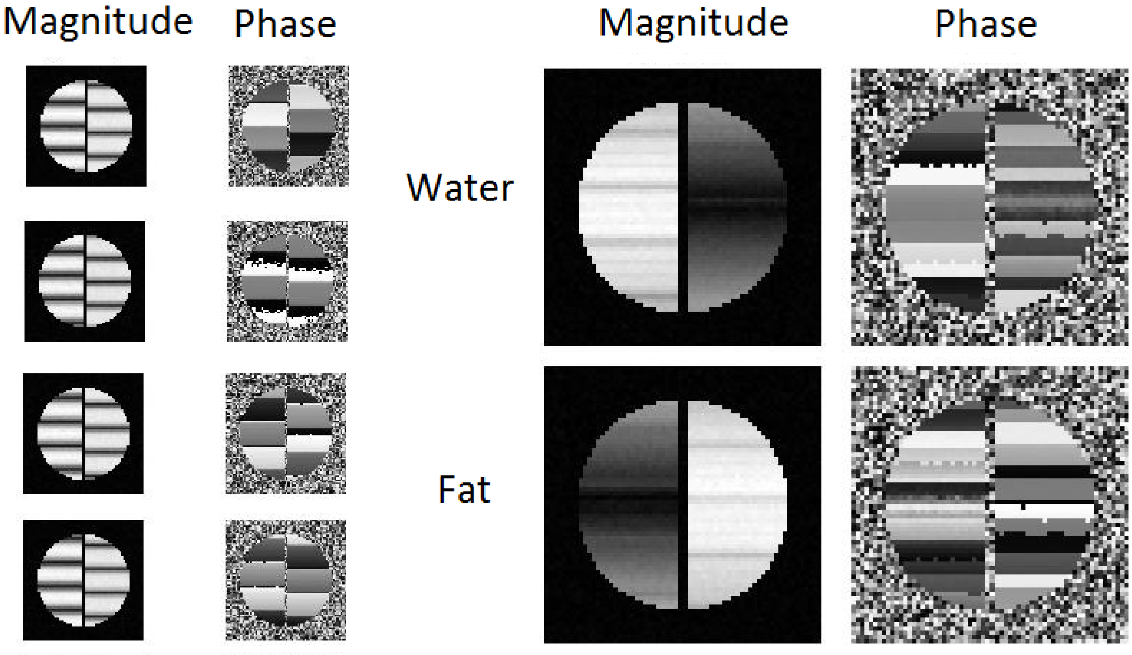

Figure 6.5: Water and fat separation using SSFP separation method in the presence of a large gradient field. (Left) Magnitude and phase of four-phase cycled SSFP images in a large gradient field. (Right) Magnitude and phase of separated water and fat images.

6.4 Discussion and Future Work

The focus of this thesis was the development of a new technique for water fat separation in MRI. This technique combines steady state free precession (SSFP) and Dixon techniques for water fat suppression in order to generate images which are free of the banding artifacts and are robust in the presence of noise and moderate B_0 inhomogeneities. At this point in time, all the work in the development and the analysis for this algorithm has been done with simulations. The simulations currently show the SSFP separation method to be a promising technique in water fat separation. However, this is not a guarantee that this will work well with real MRI data. The next step in the development of this algorithm is to test the algorithm using real data. The first planned experiment is to use a phantom of water and oil to test the algorithm. The second planned experiment would be to test the algorithm using a real person.

Appendix A

Water-Fat Separation with SSFP Algorithm Psuedo-Code

Algorithm 2 Water-Fat Separation with SSFP

```
procedure SEPARATOR($M_0$, $\alpha$, $\phi$, $\delta\phi$, $\beta$, TR, TE, $T_1$, $T_2$,$N_r$)
                                                          ▷ Generate 4 SSFP Images
    $img_1$ = SSFP($\delta\phi = 0$,      $\phi = 0$,        TE = $\frac{TR}{2} - \frac{3\Delta t_f}{2}$
    $img_2$ = SSFP($\delta\phi = \pi/2$,  $\phi = -\pi/4$,   TE = $\frac{TR}{2} - \frac{\Delta t_f}{2}$
    $img_3$ = SSFP($\delta\phi = \pi$,    $\phi = -\pi/2$,   TE = $\frac{TR}{2} + \frac{\Delta t_f}{2}$
    $img_4$ = SSFP($\delta\phi = 3\pi/2$, $\phi = -3\pi/4$,  TE = $\frac{TR}{2} + \frac{3\Delta t_f}{2}$

    for Each Pixel do
        [$s_1$,$s_2$,$s_3$] = TopThree($img_1$, $img_2$, $img_3$, $img_4$)   ▷ Select Top 3 Signal Magnitudes
        mag = ($|s_1|$ + $|s_2|$ + $|s_2|$) / 3                           ▷ Average Signal Magnitudes
        $s_1$ = mag * exp($i\angle s_1$))                                   ▷ Attach Signal Phase
        $s_2$ = mag * exp($i\angle s_2$))                                   ▷ Attach Signal Phase
        $s_3$ = mag * exp($i\angle s_3$))                                   ▷ Attach Signal Phase

                  ▷ Select Top In-Phase/Out-Phase Images for Water Fat Separation
        if TopThree are $img_1, img_2, img_3$ then
            if $|img_1| + |img_2| > |img_2| + |img_3|$ then
                Two-PointDixonSeparator($s_1$, $s_2$)
            else
                Two-PointDixonSeparator($s_2$, $s_3$)
            end if
        else if TopThree are $img_1, img_2, img_4$ then
            Two-PointDixonSeparator($s_1$, $s_2$)
        else if TopThree are $img_1, img_3, img_4$ then
            Two-PointDixonSeparator($s_3$, $s_4$)
        else if TopThree are $img_2, img_3, img_4$ then
            if $|img_2| + |img_3| > |img_3| + |img_4|$ then
                Two-PointDixonSeparator($s_2$, $s_3$)
            else
                Two-PointDixonSeparator($s_3$, $s_4$)
            end if
        end if
    end for

end procedure

procedure TWO-POINTDIXONSEPARATOR($m_1$, $m_2$)
    $\hat{m_w} = \frac{1}{2}[m_1 + m_2]$                               ▷ Estimate Water Component
    $\hat{m_f} = \frac{1}{2}[m_1 - m_2]$                                 ▷ Estimate Fat Component
    return $\hat{m_w}, \hat{m_f}$
end procedure
```

References

[1] Supriyo Bandyopadhyay. *Introduction of Spintronics*. CRC Press, 2008.

[2] Neal Bangerter. *Contrast Enhancement and Artifact Reduction in Steady-State Magnetic Resonance Imaging*. PhD thesis, Stanford, 2004.

[3] Johan Berglund. *Separation of Water and Fat Signal in Magnetic Resonance Imaging*. PhD thesis, Uppsala, 2011.

[4] W. Dixon. Simple proton spectroscopic imaging. *Radiology*, 1984.

[5] E. Schnieder G. H. Glover. Three-point dixon technique for true water/fat decomposition with b_0 inhomogeneity correction. *Journal of Magnetic Resonance in Medience*, 1991.

[6] Diego Hernando. *Joint Estimation of Water and Fat Images from Magnetic Resonance Signals*. PhD thesis, University of Illinois at Urbana-Champaign, 2010.

[7] Dwight G. Nishimura. *Principles of Magnetic Resonance Imaging*. Lulu, 2010.

[8] John Pauli. Dixon reconstruction. Class Notes, 2007.

[9] Angel R. Pineda Huanzhou Yu Ann Shimakawa Anaja C. Brau Brain A Hargreaves Garry E. Gold Jean H. Brittain Scott B. Reeder, Charles A. McKenzie. Waterfat separation with ideal gradient-echo imaging. *Journal of Magnetic Resonace Imaging*, 2007.

[10] Zhifei Wen Ann Shimakawa Huanzhou Yu Jean Brittain Garry Gold Christopher Beaulieu Norbert Pelc Scott Reader, Angel Pineda. Iterative decomposition of water and fat with echo asymmetry and least-squares estimation (ideal). *Journal of Magnetic Resonance in Medicine*, 2005.

[11] John R. Talyor. *Classical Mechanics*. University Science Books, 2005.

[12] Gary H. Glover Thomas E. Skinner. Extended two-point dixon for calculating separate water, fat, and b0 images. *Journal of Magnetic Resonance Imaging*, 1997.